Megathrust Shear Modulated by Albite Metasomatism in Subduction Mélanges

Kohtaro Ujiie[1] [iD], Kazuya Noro[1,2], Norio Shigematsu[3] [iD], Åke Fagereng[4] [iD], Naoki Nishiyama[3], Christopher J. Tulley[4] [iD], Haruna Masuyama[1,5], Yasushi Mori[6], and Hiroyuki Kagi[7] [iD]

[1]Graduate School of Science and Technology, University of Tsukuba, Tsukuba, Japan, [2]Tokyo Soil Research, Tokyo, Japan, [3]Geological Survey of Japan, National Institute of Advanced Industrial Science and Technology, Tsukuba, Japan, [4]School of Earth and Environmental Sciences, Cardiff University, Cardiff, UK, [5]Itochu Enex, Tokyo, Japan, [6]Kitakyushu Museum of Natural History and Human History, Kitakyushu, Japan, [7]Geochemical Research Center, Graduate School of Science, University of Tokyo, Tokyo, Japan

Abstract Aseismic megathrust slip downdip of the seismogenic zone is accommodated by either steady creep or episodic slow slip events (SSEs). However, the geological conditions defining the rheology of megathrust slip remain elusive. We examined exhumed subduction mélanges on Kyushu, Japan, which deformed at ∼370–500°C under greenschist to epidote-amphibolite facies conditions, comparable to warm-slab environments. The mélanges recorded fluid release and viscous shear localization associated with metasomatic reactions between juxtaposed metapelitic and metabasaltic rocks. Metasomatic reactions caused albitization of metapelite, resulting in depth-dependent changes to megathrust rheology. In a mélange deformed at ∼370°C, very fine grained reaction products (metasomatic albite) facilitated grain boundary diffusion creep at stresses of ∼45 MPa, less than those in the surrounding metabasalt. Mineralogical and chemical changes during metasomatic reactions, and their field content, imply an onset of albite metasomatism at ∼350°C. Albite metasomatism therefore potentially contributed to decreased megathrust strength around the inferred thermally controlled base of the seismogenic zone. In a mélange deformed near the mantle wedge corner at ∼500°C, metasomatic reactions promoted local quartz vein formation and localized viscous shear at slow slip strain rates, during which the coarse-grained metasomatic albite behaved as relatively rigid blocks in a viscous matrix. We suggest that albite metasomatism can facilitate changes in a megathrust slip mode with depth and may explain why slip mode changes from creep to SSEs with tremor with increasing depth.

Plain Language Summary Along tectonic plate boundaries, where one plate slips beneath another, plate movement occurs by processes including large and devastating earthquakes slipping at meters/second, very small earthquakes called tectonic tremor, slow slip events (SSEs) slipping at millimeters/day, and steady creep slipping at centimeters/year. However, the factors controlling where these different slip styles occur remain poorly understood. On Kyushu, Japan, ancient plate boundary rocks have been exposed by uplift and erosion. Our measurements of structures and rock chemistry in these rocks revealed that chemical reactions between subducted basalts and sediments may influence the plate boundary slip behavior. In rocks that deformed near ∼370°C, chemical reactions produced very fine grained rocks that caused local weakening within the plate boundary. This could explain why the plate boundary slip behavior changes from frictional to viscous near the downdip of the seismogenic zone at ∼350°C. In rocks that deformed at ∼500°C, near where slow slip and tremor events occur, chemical reactions promoted quartz vein formation that may represent tremor and localized viscous shear at faster strain rates than in surrounding rocks. This could explain the occurrence of tectonic tremors and SSEs.

1. Introduction

Subduction plate-boundary megathrusts produce the largest earthquakes on Earth. The up-dip limit of such earthquake ruptures may be close to the trench, as a result of dynamic weakening (Noda & Lapusta, 2013; Ujiie & Kimura, 2014), whereas the downdip limit of the seismogenic megathrust is inferred to occur where temperature exceeds ∼350°C or at the intersection with the serpentinized mantle wedge, whichever is shallower (Hyndman et al., 1997). The proposed thermal control on the downdip limit of megathrust earthquake nucleation has been thought to represent the onset of effective crystal plasticity in quartz (Hyndman et al., 1997) or pressure solution

creep in metasediments (Condit et al., 2022; Fagereng & Den Hartog, 2017), but remains controversial. On the other hand, geophysical studies have revealed that slow earthquakes, such as episodic tremor and slip (ETS), occur in the transition zone between the locked seismogenic zone and the deeper, stably sliding zone (Beroza & Ide, 2011; Obara & Kato, 2016; Peng & Gomberg, 2010). ETS is marked by episodic, contemporaneous occurrences of tremors, low-frequency earthquakes, and slow slip events (SSEs) with duration of days to weeks (Obara et al., 2004; Rogers & Dragert, 2003).

An interpretation of the ETS zone is that fluid overpressure promotes frictional behavior where viscous shear otherwise predominates; this can give rise to a spatial separation of the ETS zone from the seismogenic zone (Gao & Wang, 2017). This elevated fluid pressure deemed responsible for ETS around the mantle wedge corner is caused by localized slab dehydration and silica precipitation, which is favorable in warm-slab environments (Audet & Bürgmann, 2014; Fagereng et al., 2018; Tulley et al., 2022). In addition to dehydration of hydrous minerals in the subducting slab, mixing of compositionally disparate rocks under highly reactive and fluid-saturated conditions can cause metasomatic reactions that may change mineralogy (and therefore rheology) and/or release fluid, leading to brittle failure at conditions consistent with the source region of deep tremor in subduction zones (Angiboust et al., 2015; Bebout, 2007; Bebout & Penniston-Dorland, 2016; Okamoto et al., 2021; Tarling et al., 2019). In these mixed lithology (and therefore rheology) assemblages, ETS has been explained by contemporaneous failures in velocity-weakening materials and viscous shear in surrounding velocity-strengthening matrix (Ando et al., 2012; Beall et al., 2019; Behr et al., 2018; Fagereng et al., 2014; Hayman & Lavier, 2014; Skarbek et al., 2012). However, these mechanisms remain debated and may require specific conditions, and the geological conditions responsible for slow slip remain elusive.

We examine how metasomatic reactions at basalt-sediment interfaces may influence the megathrust slip style at depths near and below the base of the seismogenic zone based on our geological studies of the subduction-related Makimine and Nishikashiyama mélange shear zones on Kyushu, Japan (Figure 1). Field observations and laboratory analyses using samples from the mélanges revealed that in some locations, very fine grained metasomatic reaction products lead to a decrease in shear strength, while elsewhere, metasomatic reactions form higher viscosity coarse-grained lenses interleaved within weaker layers, leading to locally increased strain rates within the mélange. Our results suggest that viscous creep and SSEs along megathrusts may be promoted by depth-dependent metasomatic reactions in subduction mélanges.

2. Geologic Setting

The Makimine mélange in the Late Cretaceous Shimanto accretionary complex of eastern and central Kyushu (Figure 1b) records progressive subduction-related deformation and prehnite-actinolite to greenschist facies metamorphism at ∼300–350°C, comparable to the conditions near the downdip limit of the seismogenic zone in warm subduction zones (Hara & Kimura, 2008; Mackenzie et al., 1987; Palazzin et al., 2016; Tulley et al., 2022; Ujiie et al., 2018). The stratigraphic sequence of the mélange shows a repetition, possibly resulting from duplex underplating. Each sequence is ∼1–2 km-thick and shows an ocean plate stratigraphy that is composed, in ascending order, of terrigenous, metapelite-dominated mélange containing tabular lenses of metabasalt, metasandstone-metapelite mélange, and coherent, bedded metasandstone and metapelite (Needham & Mackenzie, 1988; Ujiie et al., 2018). The absence of pelagic sedimentary rocks, such as radiolarian chert, as well as relatively high-temperature metamorphic conditions of the mélange, likely represents the subduction of young and warm oceanic plate. The kinematics of the Makimine mélange, determined from stretching lineations and asymmetric fabric (e.g., S-C fabric), indicates NNW-directed subduction (Mackenzie et al., 1987; Tulley et al., 2020; Ujiie et al., 2018). These features are consistent with plate reconstruction of the Late Cretaceous paleo-Pacific margin (Müller et al., 2008; Whittaker et al., 2007).

The Nishikashiyama mélange in the Nishisonogi metamorphic rocks of western Kyushu (Figure 1c) also records subduction-related deformation under epidote-amphibolite facies metamorphic conditions (Mori et al., 2014; Nishiyama, 1989; Tulley et al., 2022). The thickness of the mélange is at least 50 m (Nishiyama, 1989). The maximum temperature of the Nishisonogi metamorphic rocks, determined from the Raman spectroscopic analysis on carbonaceous materials in the metapelite, is 440–524°C (Mori et al., 2019). The mélange contains blocks of metapelite and metabasite in a matrix composed of chlorite-actinolite schist (CAS) that is interpreted to be derived from mechanical mixing and chemical reaction between serpentinite and metabasite (Mori et al., 2014;
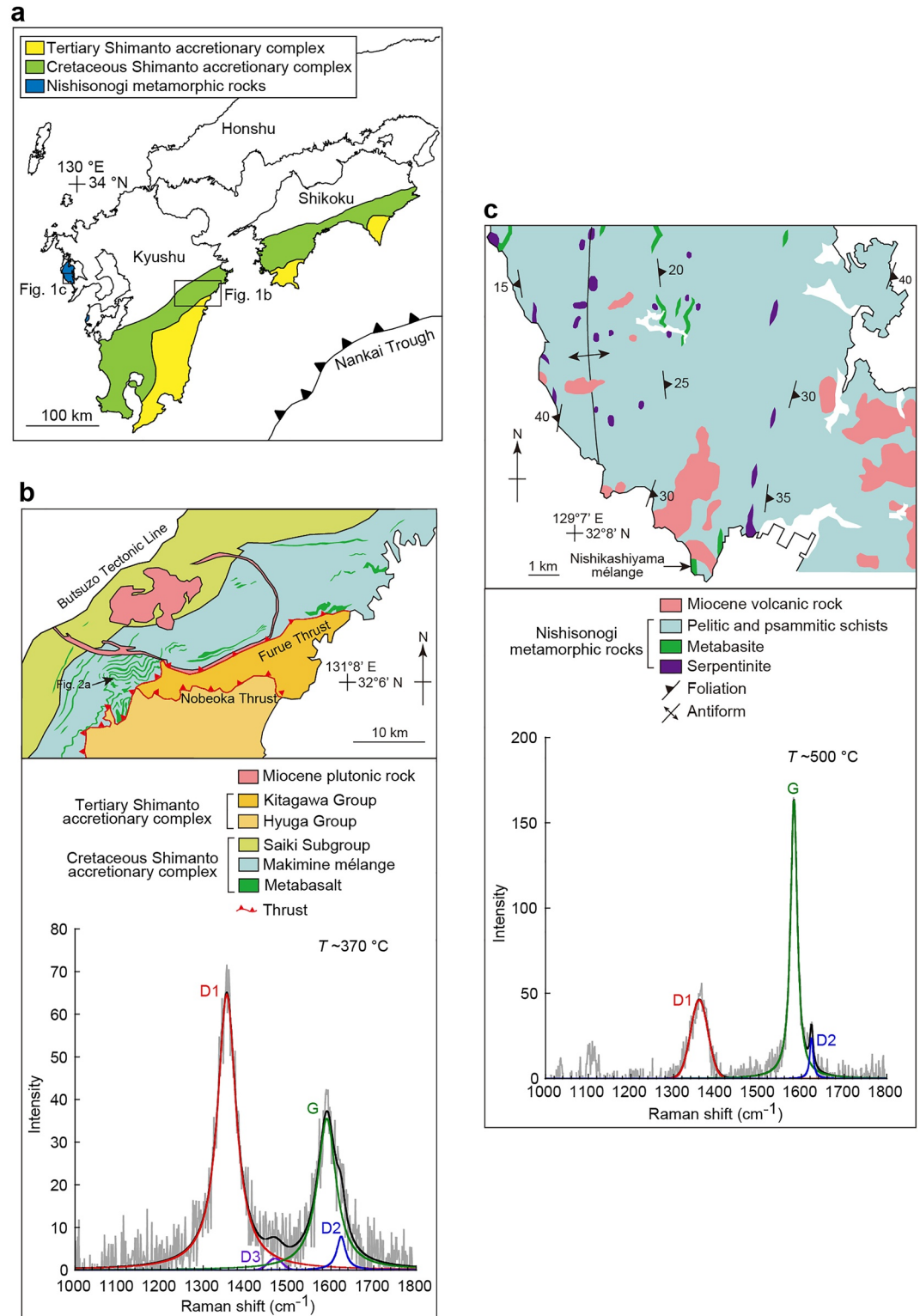
Figure 1. Geologic settings of subduction mélanges. (a) Locations of the Shimanto accretionary complex and the Nishisonogi metamorphic rocks in Kyushu. (b) Makimine and (c) Nishikashiyama mélanges with Raman spectra of carbonaceous materials with decomposed peaks.

Nishiyama, 1989, 1990). The mixed nature of sedimentary, mafic, and ultramafic rocks has led to the inference that the mélange originates from the slab-mantle interface near the mantle wedge corner (Mori et al., 2014; Nishiyama, 1989, 1990). The metamorphic ages of pelitic and psammitic schists, determined from K-Ar dating and ^{40}Ar-^{39}Ar dating, range from 85 to 60 Ma (Faure et al., 1988; Hattori & Shibata, 1982). The Nishikashiyama mélange has survived retrograde metamorphism and retained epidote-amphibolite facies mineral assemblages (Nishiyama, 1990) with the exception of some zoned amphiboles reflecting retrogression from hornblende-stable to actinolite-stable conditions, expected at near-peak metamorphic conditions (Tulley et al., 2020, 2022). The age and metamorphic conditions of the Nishisonogi metamorphic rocks are compatible with the subduction of a relatively warm oceanic plate during the Late Cretaceous as suggested by plate reconstructions (Müller et al., 2008; Whittaker et al., 2007). Overall, the exhumed mélanges on Kyushu provide an analog to modern megathrust shear-zone downdip of the seismogenic zone in warm-slab environments.

3. Methods

3.1. Raman Spectroscopic Analysis

We used the Raman carbonaceous material geothermometer for the estimation of maximum attained temperatures in subduction mélanges. For the Raman spectroscopic analysis, we used thin sections of metapelite from the mélanges. To avoid damage of carbonaceous material by mechanical polishing during thin-section preparation, carbonaceous material completely embedded within the minerals was chosen for the Raman measurements. Raman spectra of carbonaceous materials were acquired from a laser Raman microscope with a 50 × objective and a 514.5 nm Ar$^+$ laser installed at the University of Tokyo. To prevent damage of carbonaceous materials caused by an increase in the sample temperature by the incident laser (Kagi et al., 1994) and to reduce a fluorescent background, the laser power was kept at ~0.7 and ~2.0 mW for samples from the Makimine and Nishikashiyama mélanges, respectively, with an acquisition time of 30 s. We used the commercial software PeakFit 4.12 (Systat Software, Inc.) for the peak decomposition of Raman spectra. We corrected the spectra by subtracting the linear baseline in the range of 1,000–1,800 cm^{-1}. After the correction, the spectra for carbonaceous materials were decomposed with a pseudo-Voigt function (Gaussian-Lorentzian sum) into D1-, D2-, G-, D3-, and D4-bands, which have peak positions near 1,350, 1,620, 1,590, 1,510, and 1,245 cm^{-1}, respectively (Kouketsu et al., 2014; Lahfid et al., 2010).

We adopted the Raman carbonaceous material geothermometer proposed by Kouketsu et al. (2014), which is well applicable for the temperature range of 200–400°C, for the estimation of maximum attained temperature in the Makimine mélange:

$$T(^{\circ}C) = -215\,(\text{FWHM-D1}) + 478 \tag{1}$$

where FWHM-D1 is the full width at half maximum of the D1-band. The estimated temperature was 371°C with a standard deviation of 9°C (Figure 1b and Table S1 in Supporting Information S1). To estimate the maximum attained temperature for the Nishikashiyama mélange, we used the Raman carbonaceous material geothermometer proposed by Beyssac et al. (2002) applicable for temperatures higher than 400°C:

$$T(^{\circ}C) = -445\,R2 + 641 \tag{2}$$

where $R2$ is the relative area of the defect band defined by $D1/(G + D1 + D2)$. The calculated temperature was 500°C with a standard deviation of 37°C (Figure 1c and Table S2 in Supporting Information S1). For both geothermometers, the stated uncertainties are the uncertainties inherent in the calibration, which are ±30°C and ±50°C for Equations 1 and 2, respectively (see Beyssac et al., 2002; Kouketsu et al., 2014). These values are larger than the standard deviation of the measurements.

3.2. X-Ray Diffraction (XRD) and Whole-Rock Composition Analyses

To examine the change in mineralogy associated with metasomatic reactions, the XRD analysis was conducted on bulk powders from metapelite and metasomatized metapelite in the Makimine and Nishikashiyama mélanges. We used a Rigaku MiniFlex 600 XRD system with a CuKα target, an acceleration voltage of 40 kV, an electronic current of 15 mA, and a scanning speed of 0.001°s^{-1}.

To characterize the change in whole-rock chemistry associated with metasomatism, the X-ray fluorescence (XRF) analysis was performed on 1:5 dilution glass beads (Mori & Mashima, 2005), which were prepared from the powdered rock samples. The rock samples for the XRF analysis were taken across the metasomatic reaction zones in the Makimine and Nishikashiyama mélanges. Three samples were collected from >∼1 m away from the reaction zones to determine the composition of metapelite unaffected by the reaction. The volume of each sample was approximately 10^3 cm^3. We used a PANalytical MagiX Pro XRF spectrometer and a PerkinElmer 2400 II CHN element analyzer. Part of the powder sample was heated to 950°C for 3 hr to measure loss on ignition (LOI), while the unheated powder was used for the measurement of CHN (H_2O and C). Whole-rock compositions were obtained by combining XRF, LOI, and CHN data (Tables 1 and 2).

We also analyzed the chemical mass balance between the metapelite and metasomatized metapelite using an isocon method (Grant, 1986). The isocon is defined by TiO_2, Zr, Nb, and Sc, because these elements are recognized as high-field strength elements and relatively immobile during hydrothermal alterations under metamorphic conditions up to amphibolite facies (Ague, 2011; Mori et al., 2014; Rollinson, 1993). Concentrations in the isocon diagram are scaled as follows: ×0.1 for SiO_2; ×0.5 for Al_2O_3; ×1 for Fe_2O_3, Na_2O, K_2O, and C; ×2 for MgO and H_2O; ×5 for CaO; ×10 for TiO_2, MnO, and P_2O_5; ×100 for Zr and Ba; ×500 for V, Zn, Rb, Sr, and Ce; ×1,000 for Sc, Cr, Ni, Cu, Y, Nb, La, Nd, and Pb.

3.3. Electron Backscatter Diffraction (EBSD) Analyses

EBSD analyses were performed to characterize the crystallographic preferred orientation (CPO) of mineral grains and microstructural features, including grain size and intragrain distortion (Prior et al., 1999). EBSD data were acquired in a HITACHI SU-3500 scanning electron microscope (SEM) equipped with an Oxford Instruments Nordlys EBSD detector using Aztec software. The SEM is installed at the Geological Survey of Japan, National Institute of Advanced Industrial Science and Technology. The EBSD measurements were performed with an accelerating voltage of 15 kV, a working distance of 18 mm, a specimen tilted by 70°, and a low-vacuum mode (20 Pa). Before the EBSD measurement, the thin sections were polished with SYTON colloidal silica solution and not coated.

EBSD data were processed using the Oxford Instruments Channel 5 software suite. To construct maps, pixels with different orientation relative to their surroundings were removed. To construct pole figures, grains were detected using the Channel 5 Tango program. For this purpose, a misorientation of 10° is chosen to mark the change from a low-angle to a high-angle boundary. Although this angle is confirmed for quartz (Shigematsu et al., 2006; White, 1976), it has not been well constrained for other minerals (Fitz Gerald et al., 1983; Heinemann et al., 2005). The pole figures were constructed for each data set based on a subset of one point per grain. The grain sizes were calculated as the equivalent circular diameter of grains based on the area of detected grains.

4. Results

4.1. Characteristics of Metasomatic Reactions in Subduction Mélanges

4.1.1. Makimine Mélange

The greenschist facies Makimine mélange in central Kyushu preserves products of metasomatic reactions along apparent bleached boundaries between metabasalt/metadolerite and metapelite (Figures 2a and 2b). The mineral assemblage in the reaction zones is quartz + albite + muscovite + chlorite ± carbonaceous material ± actinolite. This is almost the same assemblage as in metapelites, except that the reaction zones are poor in or lack muscovite and carbonaceous materials and are enriched in albite relative to metapelite (Figures 2c and 2d). The subduction-related metapelite foliation defined by alignment of chlorite is locally preserved in the reaction zones, but is largely overprinted by very fine grained albite (Figures 2b and 2d).

In reaction zones, albite occurs as euhedral crystals with an average grain diameter of 8.6 ± 3.0 μm (Figure 3a). The normalized spider diagrams of metapelite and metasomatized metapelite denote similarities in the concentration of high-field strength elements (Nb, Zr, and Ti) that are generally immobile during alteration (Grant, 1986, 2005; Mori et al., 2014; Rollinson, 1993), suggesting that the reaction zone is derived from alteration of metapelite rather than metadolerite (Figure 3b). X-ray diffraction (XRD) patterns and isocon diagrams obtained from whole-rock major element compositions show that the metasomatism is characterized by the consumption of

Table 1
Whole-Rock Compositions and Density of Metapelite, Metasomatized Metapelite, and Metadolerite in the Makimine Mélange

Rock	Metapelite	Metasomatized metapelite			Metadolerite			
Sample No.	TS-MS	TS-RZ1	TS-RZ2	TS-RZ3	TS-DOL1	TS-DOL2	TS-DOL3	TS-DOLR
[a]Distance (cm)	[b]100	2.6	7.1	11.5	1.5	4.0	10.0	[b]100
(wt%)								
SiO_2	69.92	71.63	71.90	72.34	48.13	47.13	47.43	47.69
TiO_2	0.50	0.51	0.51	0.50	0.96	1.00	0.98	0.92
Al_2O_3	14.56	14.60	14.80	14.46	17.95	18.57	17.62	19.14
Fe_2O_3	3.53	1.12	0.56	0.75	8.76	9.15	9.00	8.07
MnO	0.06	0.01	0.01	0.01	0.14	0.15	0.14	0.13
MgO	1.08	1.42	1.47	1.49	7.54	7.70	7.38	6.98
CaO	0.79	0.95	0.92	0.86	10.24	9.82	11.60	10.82
Na_2O	2.28	7.81	7.94	7.65	2.95	2.63	2.41	2.70
K_2O	3.24	n.d.	n.d.	0.01	0.24	0.49	0.24	0.47
P_2O_5	0.07	0.10	0.08	0.07	0.09	0.09	0.09	0.08
H_2O	1.84	0.54	0.46	0.45	2.76	3.10	2.70	2.83
C	0.62	0.00	n.d.	n.d.	0.13	0.07	0.36	0.05
Total	98.49	98.69	98.64	98.59	99.90	99.89	99.95	99.88
(ppm)								
Sc	10	8	10	10	36	36	37	35
V	79	70	79	79	232	237	230	221
Cr	28	27	27	28	292	304	295	284
Ni	21	9	12	21	92	89	85	84
Cu	39	n.d.	n.d.	n.d.	79	47	77	60
Zn	98	n.d.	n.d.	n.d.	64	62	58	52
Rb	108	2	1	n.d.	10	18	9	18
Sr	119	65	105	147	150	139	141	150
Y	27	20	27	39	26	27	26	25
Zr	178	163	162	158	60	62	61	57
Nb	9	11	9	10	3	3	4	3
Ba	564	58	73	111	51	88	50	73
La	29	22	31	56	n.d.	n.d.	n.d.	n.d.
Ce	58	41	51	120	9	7	6	n.d.
Nd	28	16	18	53	n.d.	n.d.	n.d.	n.d.
Pb	24	n.d.	n.d.	n.d.	5	3	n.d.	n.d.
Density (g/cm^3)	2.70	2.66	2.63	2.65	2.79	2.95	2.93	3.12

Note. n.d., not detected.
[a]Distance from the base of the metasomatic reaction zone. [b]Approximate distance from the base of the metasomatic reaction zone.

muscovite and carbonaceous materials from the metapelite, leading to the formation of albite, increase in sodium, and decrease in potassium and carbon in the reaction zone, and release of H_2O from the system (Figures 3c and 3d). The isocon slope of 1.02 ± 0.08 indicates almost no bulk mass change during metasomatic reactions, and the silica content remained approximately constant (Figure 3d). Although the number of data points is limited, increased sodium content in the metasomatized metapelite relative to metapelite and metadolerite is evident, and the sodium contents remain the same in the reaction zone (Figure 3e). These features suggest an infiltration of sodium-bearing fluids by advection.

Table 2
Whole-Rock Compositions and Density of Metapelite, Metasomatized Metapelite, Chlorite-Actinolite Schist, and Metabasite in the Nishikashiyama Mélange

Rock	Metapelite	Metasomatized metapelite			Chlorite-actinolite schist	Metabasite			
Sample No.	NK2-MS	NK2-RZ1	NK2-RZ2	NK2-RZ3	NK2-HSZ	NK2-BBS1	NK2-BBS2	NK2-BBS3	NK2-BSR
[a]Distance (cm)	[b]100	1.7	8.1	15.9	5	46.5	51.5	56.0	[b]100
(wt%)									
SiO_2	67.89	60.95	68.20	67.71	47.81	62.13	62.16	62.52	55.17
TiO_2	0.57	0.73	0.57	0.57	0.61	0.64	0.66	0.66	0.61
Al_2O_3	14.66	17.61	14.50	14.93	9.72	16.97	16.76	16.42	16.16
Fe_2O_3	4.51	4.65	4.49	4.40	9.02	4.94	5.34	5.40	6.21
MnO	0.09	0.05	0.06	0.06	0.16	0.05	0.05	0.05	0.10
MgO	1.86	3.95	2.27	2.03	19.62	3.82	3.84	4.00	7.29
CaO	0.80	0.72	0.51	0.50	5.75	0.82	0.76	0.77	6.15
Na_2O	2.38	7.45	3.62	3.04	0.78	5.59	4.41	4.23	5.19
K_2O	3.06	0.46	2.37	2.97	n.d.	1.90	2.66	2.57	0.57
P_2O_5	0.09	0.11	0.07	0.05	0.10	0.15	0.14	0.14	0.12
H_2O	2.08	2.26	2.11	2.26	6.42	2.02	2.51	2.71	2.22
C	0.56	0.00	0.04	0.32	0.05	0.05	0.04	0.06	n.d.
Total	98.55	98.94	98.81	98.85	100.05	99.08	99.31	99.53	99.78
(ppm)									
Sc	12	14	11	12	21	17	17	15	22
V	91	103	85	87	122	132	137	138	152
Cr	58	75	61	64	1,024	59	51	46	313
Ni	7	46	40	29	834	35	36	30	143
Cu	n.d.	48	73	20	n.d.	74	72	63	23
Zn	73	53	65	71	99	95	98	110	54
Rb	109	13	65	89	n.d.	43	58	54	10
Sr	114	51	32	35	25	48	45	48	278
Y	25	34	26	27	15	20	21	20	16
Zr	138	167	148	139	61	102	111	115	80
Nb	10	12	9	9	4	6	6	5	3
Ba	446	77	343	429	n.d.	226	307	290	46
La	22	34	27	28	7	8	9	8	7
Ce	57	70	63	59	7	20	21	22	11
Nd	21	27	24	26	8	11	10	8	6
Pb	42	12	14	15	n.d.	n.d.	n.d.	n.d.	n.d.
Density (g/cm³)	2.74	2.72	2.74	2.69	2.78	2.78	2.67	2.58	2.82

Note. n.d., not detected.
[a]Distance from the base of the metasomatic reaction zone. [b]Approximate distance from the base of the metasomatic reaction zone.

4.1.2. Nishikashiyama Mélange

In the Nishikashiyama mélange, reaction zones are observed along the boundaries between tabular metapelite lenses and CAS (Figures 4a and 4b). The thickness of reaction zones and CAS varies from ~2 to 15 cm (mostly ≤5 cm) and from ~2 to 60 cm, respectively, and both can be traced for ≤250 m, limited by outcrop exposure. The mineral assemblage of the reaction zones is quartz + albite + muscovite + chlorite ± titanite ± carbonaceous material ± epidote. This is the same assemblage as in the metapelites, except that muscovite and
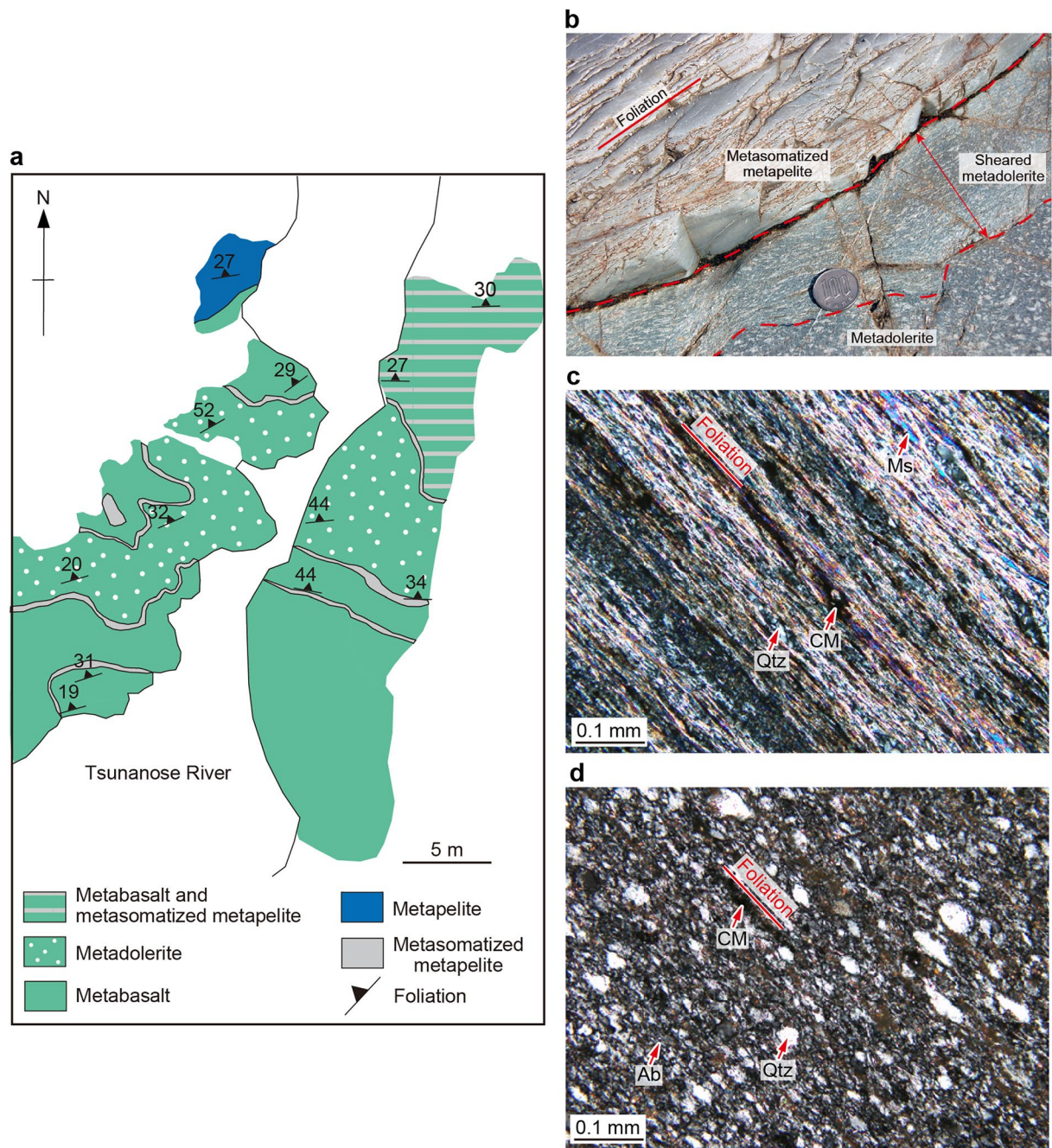
Figure 2. Occurrence of metasomatic reactions in the Makimine mélange. (a) Metasomatized metapelite intercalated in metabasalt/metadolerite exposed along Tsunanose River in central Kyushu. (b) Metasomatic reaction zones between metadolerite and metapelite. (c) Foliated metapelite defined by alignment of muscovite (Ms) and carbonaceous material (CM). Qtz: Quartz. (d) Metasomatized metapelite. Foliation is overprinted by very fine grained albite (Ab).

carbonaceous materials are rare in the reaction zone (Figure 4c), whereas the albite content increases from 15 to 37 vol% to 43–69 vol% (Mori et al., 2014).

The albite in the reaction zones occurs as ~1–2-mm-long porphyroblasts containing aligned muscovite inclusions (Figures 4c, 4d and 5a) and fluid inclusions along healed cracks (Figure 4d). Mori et al. (2014) recognized two-phase inclusions that are rich in CH_4 ($\pm CO_2$) and H_2O. As in the case of the Makimine mélange, the spider diagram shows similarities in the concentration of high-field strength elements between metapelite and metasomatized metapelite (Nb, Zr, and Ti), suggesting that the reaction zone originated from metapelite alteration
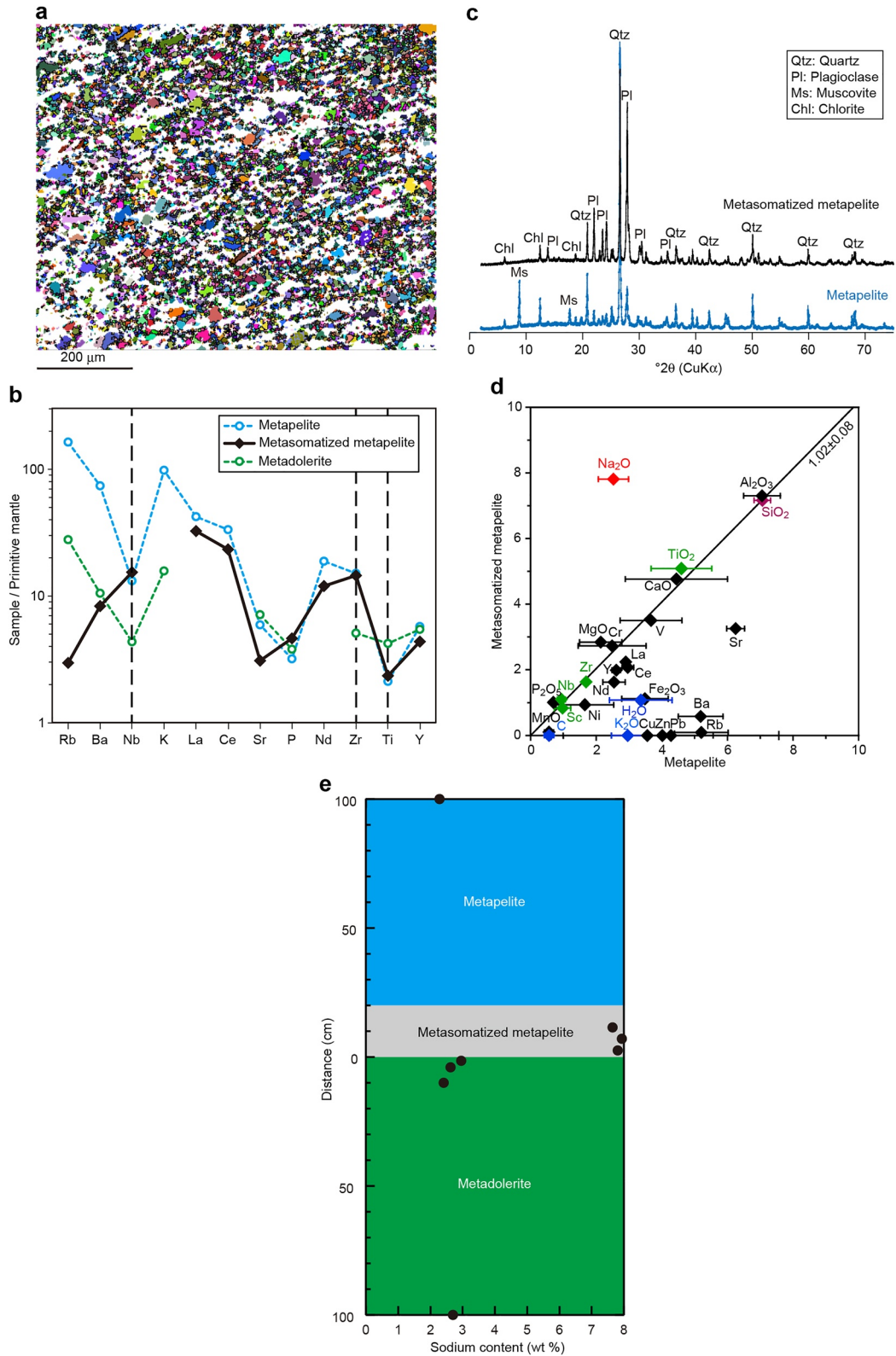
Figure 3.

(Figure 5b). XRD patterns and isocon diagrams indicate the formation of albite, consumption of muscovite and carbonaceous material, and H_2O release in the reaction zones (Figures 5c and 5d). The isocon slope of 1.18 ± 0.04 indicates ~14% volume decrease associated with silica and H_2O release during metasomatic reactions in the Nishikashiyama mélange (Figure 5d).

The sodium-concentration profile across the metasomatic reaction zone appears to reflect diffusional exchange between the metasomatized metapelite and CAS (Figure 5e). This suggests a chemical potential gradient between metapelite and CAS. Here, the mass change in sodium associated with metasomatism, ΔM_{Na} (kg m^{-3}), was calculated following Baumgartner and Olsen (1995).

$$\Delta M_{Na} = C_{Na}{}^A \rho^A \left(V^O + \Delta V \right) - C_{Na}{}^O \rho^O V^O \tag{3}$$

where C_{Na} is the concentration of sodium in the rock (kg kg^{-1}), ρ is the rock density (kg m^{-3}), and V^O is the rock volume (1 m^3). ΔV is the volume change associated with metasomatism defined by $\Delta V = \rho^O/\rho^A b$ (m^3 m^{-3}), in which b is the slope of the isocon. Superscripts O and A represent the rock before and after the metasomatism, respectively, and the calculation assumes that the metasomatized rock and the assumed protolith had the same composition prior to metasomatism. Values used in this calculation are listed in Table 3. The gain of sodium in metasomatized metapelite with a thickness of ~2–5 cm was estimated to be 2.8–7.0 kg m^{-2} by the product $\Delta M_{Na} \times z$, where z is the thickness of metasomatized zone. The total amount of released sodium from ~2 to 60-cm-thick layers of CAS is estimated to be 1.7–50.0 kg m^{-2}. Therefore, the metasomatic reactions could have produced more sodium than required to grow metasomatic albite in the metapelite. In this case, the excess sodium may migrate out of the reaction zone by advection, for example, migration of sodium-bearing fluid along permeable, foliated rocks (Kawano et al., 2011).

4.2. Link Between Metasomatic Reactions and Deformation in Subduction Mélanges

4.2.1. Makimine Mélange

Metasomatic reaction zones are accompanied by localization of viscous shear. In the Makimine mélange of central Kyushu, albite metasomatism is recognized in the metapelite that is in contact with metabasalt/metadolerite (Figures 2a and 2b). NNW-plunging lineations defined by the stretched albite occur on interfaces between metasomatized metapelite and metabasalt/metadolerite (Figures 6a and 6b). The metadolerite within a few centimeters from metasomatized metapelite shows localized viscous deformation marked by stretched plagioclase (Figure 2b). An ~0.5–2-mm-thick zone of strong shape-preferred orientation (SPO) and crystallographic-preferred orientation (CPO) in actinolite and epidote is also found along the contact between metadolerite and metasomatized metapelite (Figures 6c–6e). In the metasomatized metapelite adjacent to the contact with metabasalt/metadolerite, actinolite wraps around albite and quartz grains, some of which have sigmoidal shapes, indicating reverse sense of shear (Figure 6f). In contrast to actinolite and epidote, albite in metasomatized metapelite lacks CPO (Figure 6g).

Quartz veins in metasomatized metapelite are subparallel to the boundary between metasomatized metapelite and metabasalt/metadolerite. Deformation microstructures of quartz veins indicate dominant subgrain rotation recrystallization with local bulging recrystallization (Figures 7a and 7b). Electron backscatter diffraction (EBSD) mapping of quartz shows that low-angle boundaries (<10°) are common, indicative of subgrain rotation recrystallization (Figure 7c). Quartz c-axes show a Type-I crossed girdle that is compatible with a reverse shear sense (Figure 7d). Subgrain rotation recrystallization and bulging recrystallization are also recognized in quartz veins in metapelite outside metasomatized metapelite (Figures 7e and 7f). The kinematics of viscous shear in the reaction zones, determined from NNW-plunging lineations, asymmetric fabric formed by viscous shear, and CPO patterns of quartz c-axes, are compatible with low-angle thrust faulting associated with megathrust shear.

Figure 3. Characteristics of albite metasomatism in the Makimine mélange. (a) Electron backscatter diffraction (EBSD) map of albite in the metasomatized metapelite. Points in EBSD maps are color coded according to the three Euler angles. (b) Spider diagrams of metapelite, metasomatized metapelite, and metadolerite normalized by primitive mantle. Major and trace element data are derived from whole-rock compositions in Table 1. Broken lines indicate immobile elements used for isocon diagrams in Figure 3d. Primitive mantle values are from Sun and McDonough (1989). (c) X-ray diffraction patterns of metapelite and metasomatized metapelite. (d) Isocon diagram for metasomatized metapelite. Error bars represent standard deviations from the data of three metapelite samples. Green diamonds define the isocon. Red and blue diamonds denote the gain of Na_2O and loss of K_2O, C, and H_2O during metasomatism, respectively. Purple diamond indicates nonrelease of SiO_2 during metasomatism. (e) Sodium concentration profile across the metasomatized metapelite.
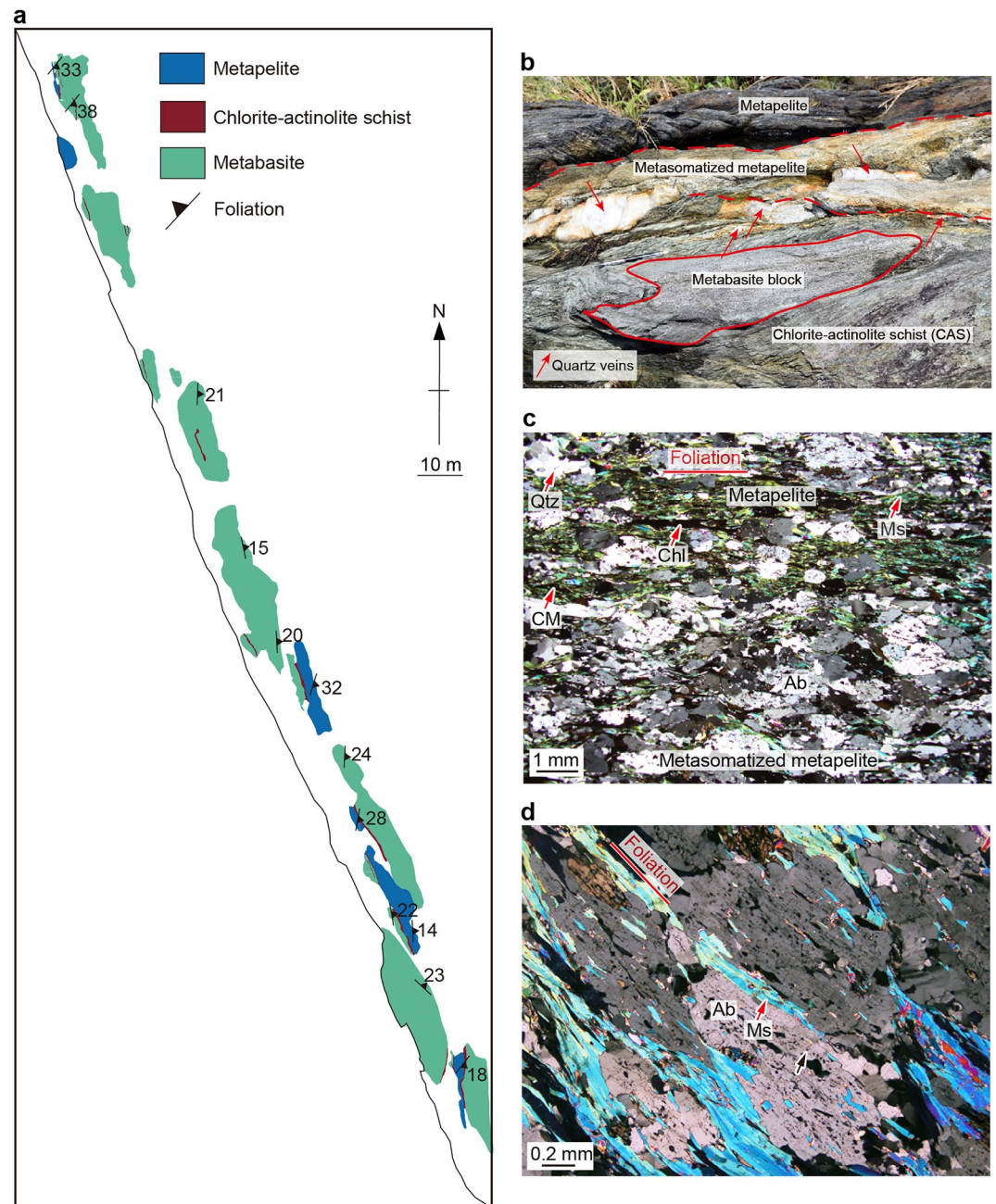
Figure 4. Occurrence of metasomatic reactions in the Nishikashiyama mélange. (a) Intercalated metabasite and metapelite in the Nishikashiyama mélange exposed along seacoast in western Kyushu, where metasomatized metapelite occurs along chlorite-actinolite schist (CAS) layers that typically separate metapelite and metabasite. (b) Metasomatic reaction zones between CAS and metapelite. (c) Photomicrograph showing upward change from metasomatized metapelite to metapelite. Ab: Albite, CM: Carbonaceous material, Chl: Chlorite, Ms: Muscovite, Qtz: Quartz. (d) Albite (Ab) porphyroblasts containing muscovite (Ms) grains with long axes parallel to the foliation. Black arrow indicates fluid inclusion.

4.2.2. Nishikashiyama Mélange

The Nishikashiyama mélange comprises intercalated pelitic and psammitic schists of the Nishisonogi meta-morphic rocks (Figure 1c). Localization of viscous shear is recognized along ~2–60-cm-thick layers of CAS that separates metasomatized metapelite and metabasite (Figure 8a). Slivers of metasomatized metapelite are incorporated into the sheared CAS (Figure 8b). CAS has a composite planar fabric showing *S–C* geometry
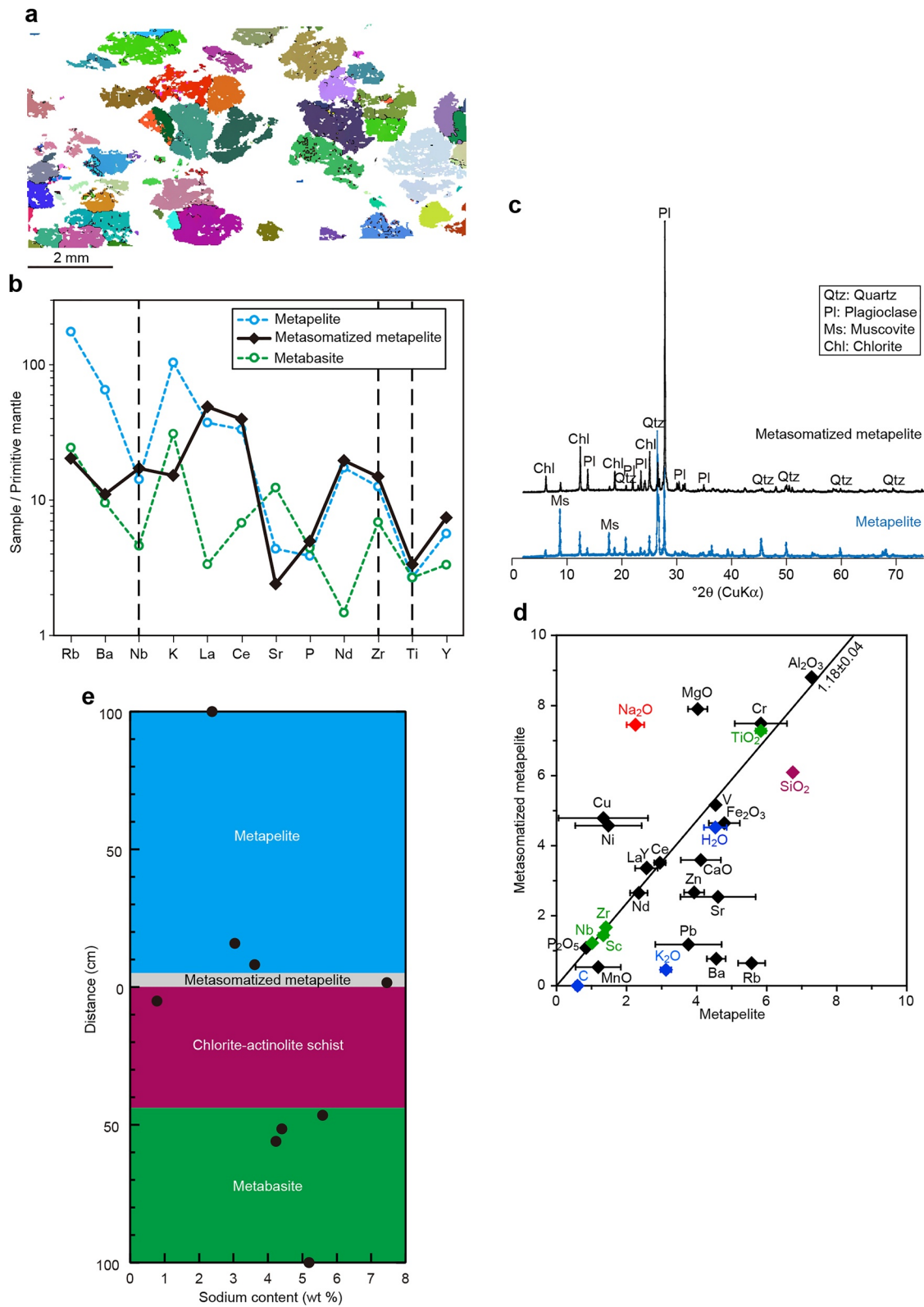
Figure 5.

Table 3
The Values Used for Mass Change Calculation

	C_{Na}^{Oa}	C_{Na}^{Aa}	ρ^{Ob}	ρ^{Ab}		ΔM_{Na}	Thickness
	kg kg^{-1}	kg kg^{-1}	g cm^{-3}	g cm^{-3}	b	kg m^{-3}	cm
Metasomatized metapelite	0.023	0.075	2.70	2.66	1.18	110	2–5
CAS	0.037	0.0078	2.80	2.78	1.08	−83	2–60

[a]measured by X-ray fluorescence. [b]measured by pycnometer.

(Figures 8a and 8c) and asymmetric folds. Actinolite and chlorite in CAS have strong SPO and CPO along *S* surfaces (Figures 8d and 8e).

Quartz veins are viscously deformed within CAS (Figure 9a), whereas they cut the metasomatized metapelite (Figure 4b), representing repetition of fracture, quartz precipitation, and viscous shear. In CAS, vein quartz is characterized by the subgrain rotation recrystallization microstructure (Figures 9b and 9c) and a quartz CPO with c-axis maxima subparallel to the shear direction (Figure 9d). In the metapelite, vein quartz misorientation angles are small within grains larger than 100 µm, and some grain boundaries show 120° triple junctions, features that imply grain boundary migration (Figures 9e and 9f). The quartz grains with 120° triple junctions also exhibit c-axis maxima perpendicular to the foliation, indicating basal *<a>* slip (Figure 9g). Deformed quartz veins in adjacent metabasite show grain boundary migration recrystallization microstructures with CPO indicating rhomb *<a>* slip, consistent with deformation at ∼500°C (Tulley et al., 2020). The shear sense indicated by CPO patterns of quartz c-axes in CAS is compatible with a top-to-the-south sense of shear determined from lineations on *C* surfaces and asymmetric fabrics (Figures 8 and 9). The foliations in the Nishikashiyama mélange dip gently eastward because of later regional-scale folding about a north-south-trending hinge line (Figure 1c). When the effect of later folding is removed by restoring foliation to horizontal, CAS shows southward-directed viscous shear compatible with inferred northward-directed subduction along the Late Cretaceous paleo-Pacific margin (Müller et al., 2008; Whittaker et al., 2007).

5. Discussion

5.1. Albite Metasomatism in Subduction Mélanges

The characteristics of reaction zones in metapelite in both mélanges indicate metasomatic albite growth that can be generalized as muscovite + Na = albite + K + H$_2$O. In the Makimine mélange, along reaction zones, the subduction-related foliation is largely overprinted by metasomatic albite (Figures 2b and 2d). However, subduction-related, NNW-plunging lineations occur near the boundaries between metasomatized metapelite and metabasalt/metadolerite (Figures 6a and 6b), suggesting that albitization occurred during the final stages of subduction-related shear. Albitite reaction zones are absent between metapelite and metabasalt in the Makimine mélange of eastern Kyushu, which experienced peak metamorphic temperatures of 328 ± 30°C (Ujiie et al., 2018), whereas albite metasomatism was recorded in the mélange in central Kyushu, showing peak temperatures of 371 ± 9°C (Figure 1b and Table S1 in Supporting Information S1).

Experimental hydrothermal alteration of graywacke in the presence of 4 mol kg^{-1} NaCl has demonstrated that albitization of illite, which can likely serve as a proxy for the albitization of muscovite, can occur at 350°C (Rosenbauer et al., 1983). The chemical composition of the graywacke after the reaction indicated the enrichment of sodium and depletion of potassium, consistent with conversion of illite to albite; consistent with this observation, the hydrothermal fluid had reduced sodium and increased potassium levels after the reaction. Nearly all potassium in the graywacke was released to the fluid within 10 days, suggesting rapid albitization of illite at

Figure 5. Characteristics of albite metasomatism in the Nishikashiyama mélange. (a) Electron backscatter diffraction (EBSD) map of albite in the metasomatized metapelite. Points in EBSD maps are color coded according to the three Euler angles. (b) Spider diagrams of metapelite, metasomatized metapelite, and metabasite normalized by primitive mantle. Major and trace element data are derived from whole-rock compositions in Table 2. Broken lines indicate immobile elements used for isocon diagrams in Figure 5d. Primitive mantle values are from Sun and McDonough (1989). (c) X-ray diffraction patterns of metapelite and metasomatized metapelite. (d) Isocon diagram for metasomatized metapelite. Error bars represent standard deviations from the data of three metapelite samples. Green diamonds define the isocon. Red and blue diamonds denote gain of Na$_2$O and loss of K$_2$O, C, and H$_2$O during metasomatism, respectively. Purple diamond indicates release of SiO$_2$ during metasomatism. (e) Sodium concentration profile across the metasomatized metapelite.
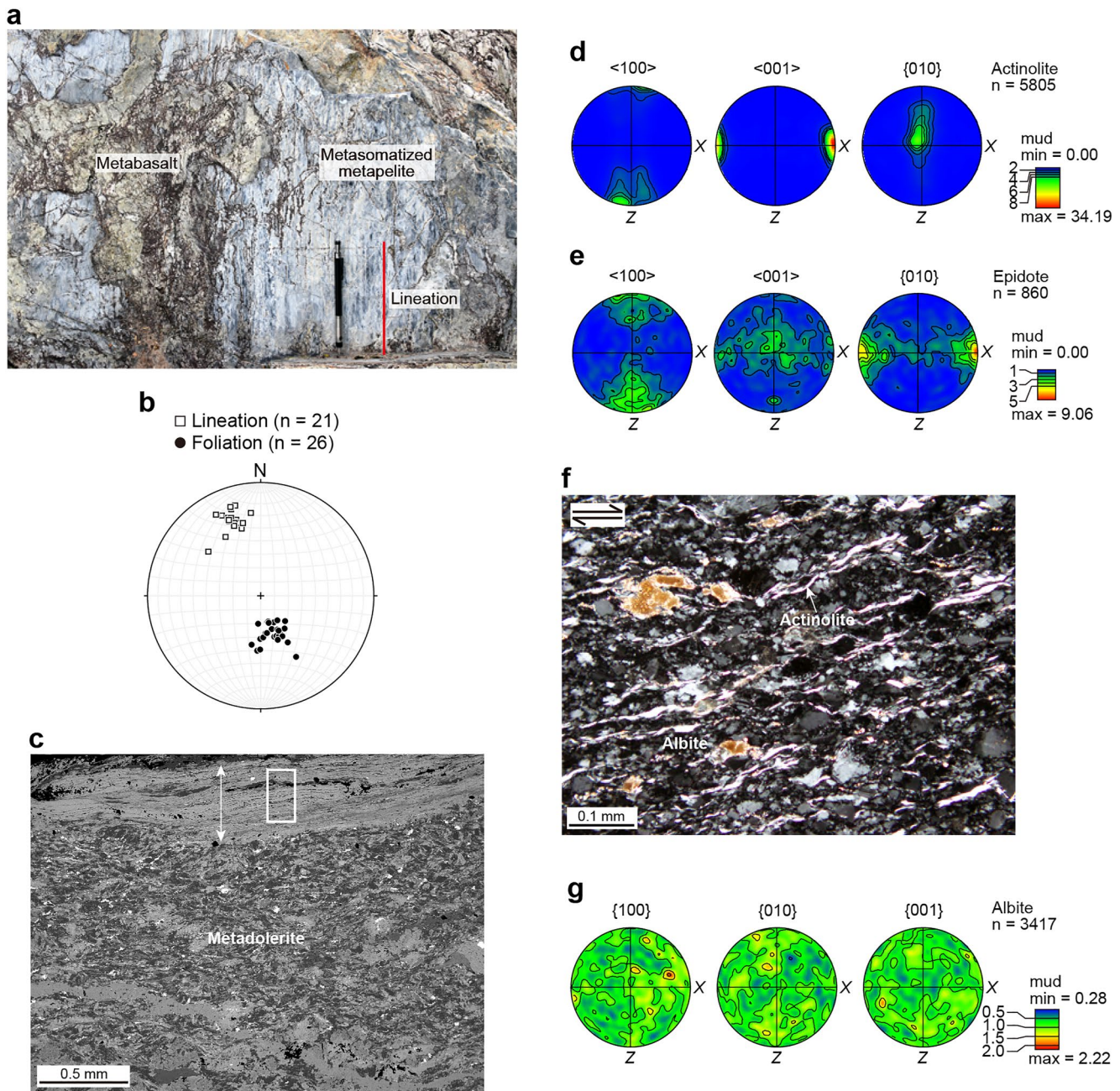
Figure 6. Metasomatism-related deformation in the Makimine mélange. (a) Lineation (red line) developed at the boundary of metasomatized metapelite and metabasalt. (b) Stereoplots of lineations and poles to foliations. (c) Backscattered electron image of the shear localization zone (double white arrows) composed of actinolite and epidote. The white rectangle shows the location where pole figures of actinolite (d) and epidote (e) are obtained. (f) Photomicrograph (cross-polarized light) of the metasomatized metapelite. Half arrows indicate the shear sense. (g) Pole figures of albite.

350°C (Rosenbauer et al., 1983). In contrast, the changes in chemical and fluid compositions were minimal in hydrothermal experiments on basalt under the same conditions as the graywacke (Rosenbauer et al., 1983). These results align with the mineralogical and chemical changes that accompany the albite metasomatism of metapelite reported here. The hydrothermal experimental result showing the albitization of illite at 350°C, coupled with the observed albitization that occurred at temperatures >328 ± 30°C but ≤371 ± 9°C, suggests that albite metasomatism occurred around the thermally inferred base of the seismogenic zone (at ~350°C, Hyndman et al., 1997).
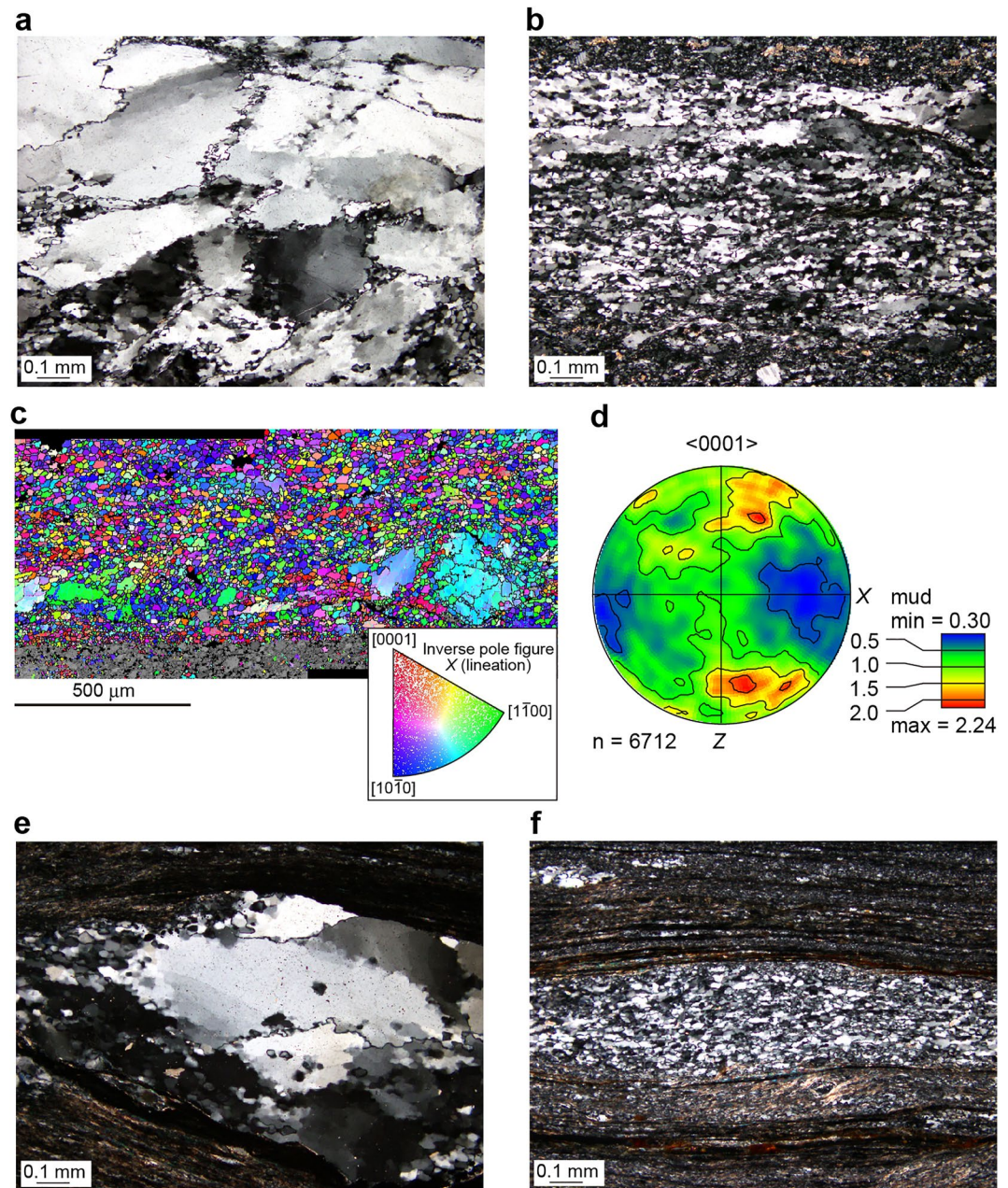
Figure 7. Quartz deformation in the Makimine mélange. Photomicrographs (cross-polarized light) of quartz veins in the metasomatized metapelite showing bulging (a) and subgrain rotation (b) recrystallization microstructures. (c) Electron backscatter diffraction map of quartz vein in the metasomatized metapelite. (d) Pole figures of quartz in (c). Photomicrographs (cross-polarized light) of quartz veins in the metapelite outside the metasomatized metapelite showing bulging (e) and subgrain rotation (f) recrystallization microstructures.

In the Nishikashiyama mélange, albite metasomatism is recognized along the boundary between metapelite and CAS, where CAS likely derived from the mixing of serpentinite and metabasite near the mantle wedge corner (Mori et al., 2014; Nishiyama, 1989, 1990). Albite porphyroblasts in reaction zones contain aligned muscovite inclusions subparallel to muscovite defining metapelite foliation around the albite grains (Figure 4d). Albitized metapelite was locally incorporated into CAS showing megathrust shear sense (Figure 8). These features suggest that albitization occurred after or during the development of mélange foliation at depths below Moho, but prior to exhumation.
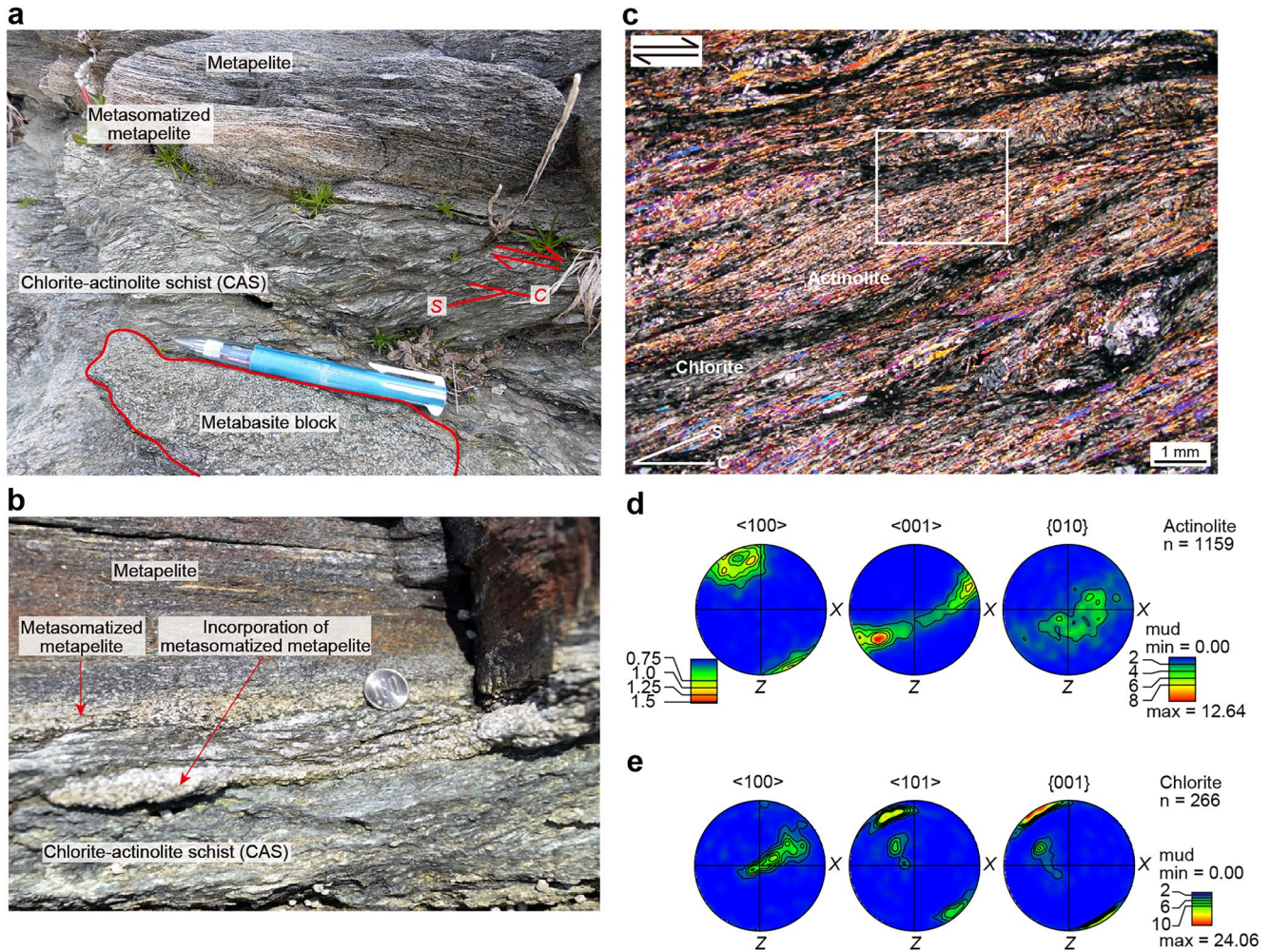
Figure 8. Metasomatism-related deformation in the Nishikashiyama mélange. (a) *S-C* fabric in shear zone composed of chlorite-actinolite schist (CAS). Red half arrows indicate the shear sense. (b) The metasomatic reaction zone between metapelite and CAS, showing incorporation of metasomatized metapelite into CAS. (c) Photomicrograph of the CAS showing *S-C* fabric. Half arrows indicate the shear sense. The white rectangle shows the location where pole figures of actinolite (d) and chlorite (e) were obtained.

We evaluated the effects of pH and sodium concentrations in the fluid on albite metasomatism, using the activity diagram of (a_{Na+}/a_{H+}) versus (a_{K+}/a_{H+}), where a_i is the activity of ion i (Figure 10). In the evaluation, we used pressures of 0.382 and 0.255 GPa for the Makimine mélange in central and eastern Kyushu, respectively (we assumed rock density of 2,600 kg m^{-3} at depths of 10 and 15 km) (Toriumi & Teruya, 1988). We adopted 1 GPa for the Nishikashiyama mélange, which is an average pressure of epidote-amphibolite facies metamorphism at $500 \pm 50°C$. When constructing the activity diagram for the seismogenic zone conditions, we assumed the temperature and pressure conditions of the Mugi mélange in the Shimanto accretionary complex, which was deformed at 200°C and 0.13 GPa (Matsumura et al., 2003). Considering the occurrence of albitization at temperatures >330°C but ≤370°C, the (a_{Na+}/a_{H+}) and (a_{K+}/a_{H+}) of the fluid at 370°C were within the stability field of albite, whereas (a_{Na+}/a_{H+}) and (a_{K+}/a_{H+}) of the fluid at 330°C were within the muscovite stability field (light blue area in Figures 10a and 10b). Both conditions were satisfied only when the (a_{Na+}/a_{H+}) of the fluid ranged within $10^{4.6–5.1}$ (dark blue area in Figures 10a and 10b). Fluid inclusion investigations suggested that a_{Na+} for the Makimine mélange is comparable to or higher than that of seawater (Nishiyama et al., 2020). By using $a_{Na+} = 4.8 \times 10^{-1}$ M (seawater value) and $(a_{Na+}/a_{H+}) = 10^{4.6–5.1}$, pH values of 4.9–5.4 were obtained. The a_{Na+} of fluid in the seismogenic zone is similar to the seawater value (Raimbourg et al., 2018; Yardley & Graham, 2002). Experimental studies on sediments/seawater interactions showed that pH did not notably change at 200–350°C (pH 5.1–5.6, Rosenbauer et al., 1983; You & Gieskes, 2001). Thus (a_{Na+}/a_{H+}) in the seismogenic zone ($T < 350°C$) is similar
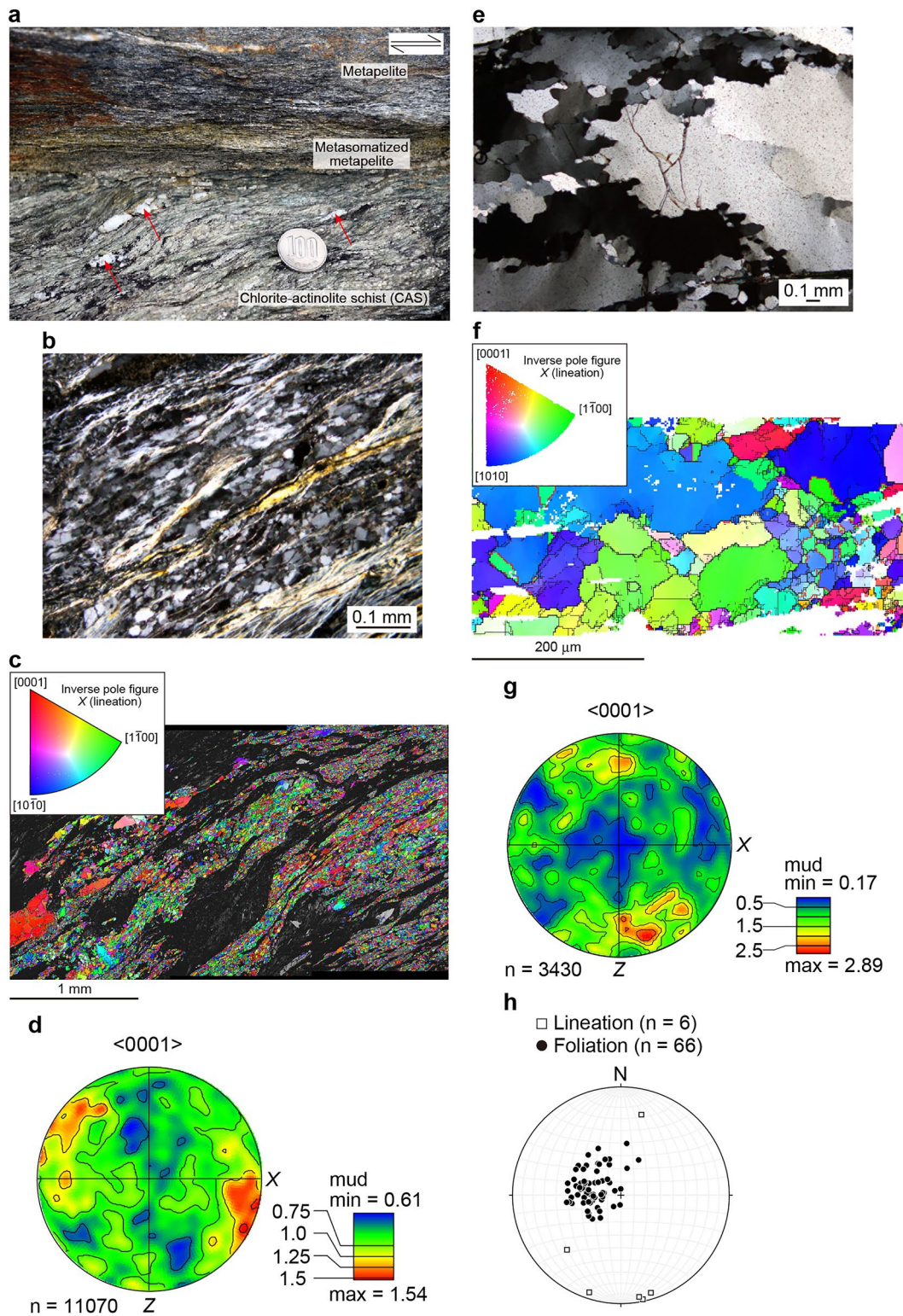
Figure 9. Quartz deformation in the Nishikashiyama mélange. (a) Asymmetrical deformation of quartz veins (red arrows) by viscous shear along chlorite-actinolite schist (CAS). Half arrows indicate the shear sense. (b) Photomicrographs (cross-polarized light) of quartz veins in CAS showing subgrain rotation recrystallization microstructures. (c) Electron backscatter diffraction (EBSD) map of quartz vein in CAS. (d) Pole figures of quartz in (c) showing the *X*-maximum quartz c-axis fabric. (e) Photomicrographs (cross-polarized light) of quartz vein in the metapelite showing grain boundary migration recrystallization. (f) EBSD map of vein quartz from the metapelite, where points are color coded according to the inverse pole figure of *X* (lineation) in the inset. Thick and thin lines indicate boundaries with misorientations larger and smaller than 10°, respectively. (g) Pole figure of quartz in a vein within the metapelite. (h) Stereoplots of lineations in CAS and mélange foliations.
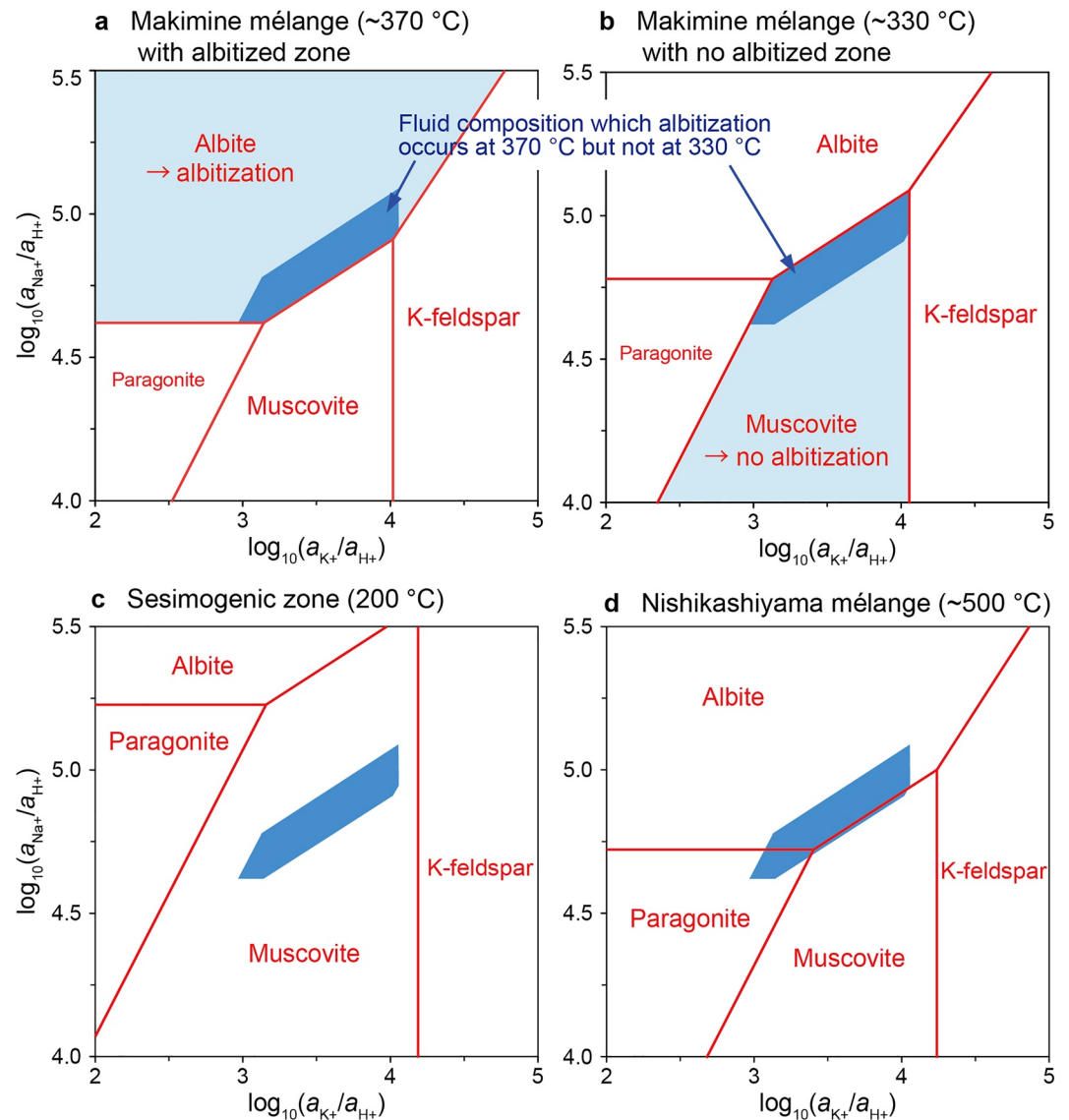
Figure 10. Activity diagram of (a_{Na+}/a_{H+}) and (a_{K+}/a_{H+}) in fluids for the Makimine and Nishikashiyama mélanges (a, b, and d) and seismogenic zone (c), showing the stability relation among different minerals. Equilibrium constants required for creating activity diagrams were calculated using the SUPCRT92 software (Johnson et al., 1992).

to that in the Makimine mélange. In this case, the albitization of muscovite is not expected in the seismogenic zone, because (a_{Na+}/a_{H+}) lies within the muscovite stability field (Figure 10c). In contrast, muscovite is likely albitized at the peak temperature of the Nishikashiyama mélange (~500°C), because (a_{Na+}/a_{H+}) plots within the albite stability field (Figure 10d). These calculations and field observations imply a thermally controlled onset of albitization of muscovite between 330 and 370°C at natural conditions of warm-slab subduction.

The albite metasomatism in the Maikime mélange suggests a fluid out of equilibrium with the wall rocks (Figure 3e). Externally derived fluids are supported by quartz veins, which require extensive fluid flow through the mélange (Nishiyama et al., 2020; Tulley et al., 2022). The fluid source would have involved local as well as downdip dehydration reactions, particularly in the subducting slab (Tulley et al., 2022), as well as mantle-derived fluids (Nishiyama et al., 2020). While the volume of fluid is not constrained, fluid flow along the plate interface could drive metasomatism, which is consistent with these previous studies invoking plate interface-parallel flow of mixed-source fluids.

Table 4
Flow Law Parameters Used in This Study

Flow law	A (MPa^{-n} s^{-1})	m	Q (kJ mol^{-1})	n
Hirth et al. (2001)	6.30957×10^{-12}	1	135	4
Offerhaus et al. (2001)	log A (MPa^{-n} μm^m s^{-1})			
Dislocation creep regime	3.4	0	332	3
Diffusion creep regime	3.9	3	193	1

5.2. Shear Strength of Metasomatism-Related Viscous Shear Zone

To determine shear strength during metasomatism-related viscous shear in the Makimine mélange, the recrystallized quartz grain size (D) in a quartz vein in metasomatized metapelite was calculated from EBSD data, which yielded 12.5 ± 6.3 μm. Then, the differential stress (σ) was estimated using a recrystallized grain size piezometer for quartz (Stipp & Tullis, 2003):

$$D = 10^{3.56}\sigma^{-1.26} \tag{4}$$

Where σ was divided by 2 to give maximum shear stress in the range of 33–78 MPa (average 45 MPa). The strain rate ($\dot{\varepsilon}$) was determined by a quartz flow law of Hirth et al. (2001):

$$\dot{\varepsilon} = A f_{H2O}^m \sigma^n \exp(-Q/RT) \tag{5}$$

Flow law parameters for quartz are shown in Table 4. We used a water fugacity at 0.382 GPa (Toriumi & Teruya, 1988) and 370°C for the Makimine mélange. The stress values estimated from the quartz piezometer then give strain rates of 8.0×10^{-14}–2.7×10^{-12} s^{-1} (average 2.9×10^{-13} s^{-1}). Development of quartz veins subparallel to boundaries of reaction zones and lack of boudinaged quartz veins in reaction zones suggest a small viscosity contrast between quartz veins and surrounding metasomatic albite. Assuming that the deformation of albite in metasomatic reaction zones occurred at the same shear stress and strain rate as quartz dislocation creep, we made a deformation mechanism map for wet albite (Figure 11), using the wet albite flow law for diffusion or dislocation creep (Offerhaus et al., 2001) (see Table 4 for flow parameters):

$$\dot{\varepsilon} = A \sigma^n d^{-m} \exp(-Q/RT) \tag{6}$$

The measured albite grain size (8.6 ± 3.0 μm) is compatible with a preference for grain boundary diffusion creep over dislocation creep (Figure 11). This result, and the microstructural observations of quartz and albite in the metasomatic reaction zones, suggests coeval quartz dislocation creep and albite grain boundary diffusion creep
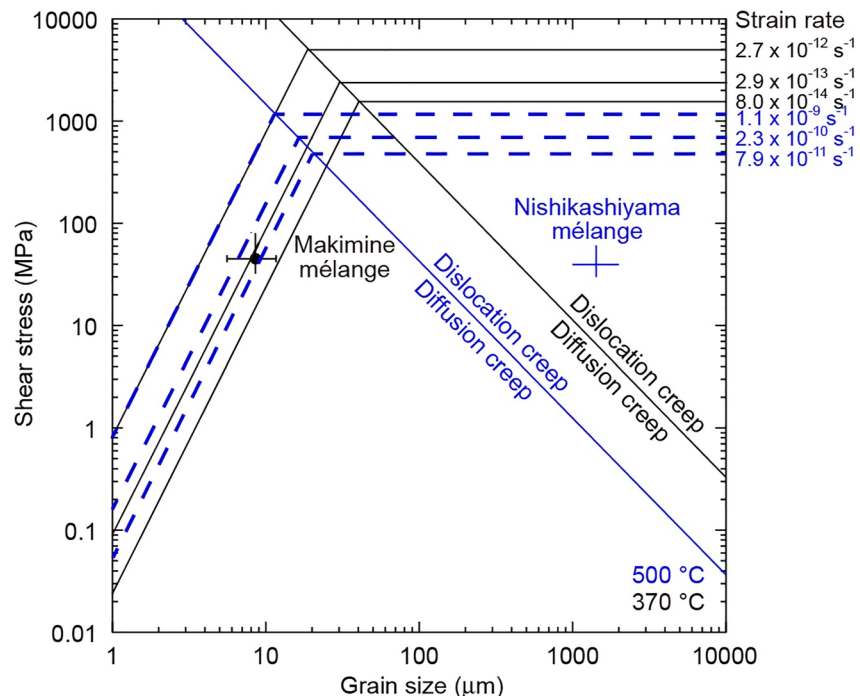

Figure 11. Deformation mechanism map for wet albite. Shear stresses of the Makimine and Nishikashiyama mélanges are determined from recrystallized quartz grain size piezometry (Stipp & Tullis, 2003). Black line and dashed blue line indicate the strain rates of the Makimine mélange at 370°C and the Nishikashiyama mélanges at 500°C, respectively.

at the peak metamorphic conditions experienced by the Makimine mélange. The calculated stress and strain rate ranges overlap with, but are somewhat lower and slower than, the 43–94 MPa driving stress and $\sim 10^{-12}$ s^{-1} strain rate derived for distributed shear in the surrounding metabasalt (Tulley et al., 2020).

Metasomatism-related viscous shear is localized along CAS in the Nishikashiyama mélange. The quartz veins in CAS show deformation by subgrain rotation recrystallization and recrystallized quartz grain size of 14.7 ± 5.8 μm. Considering recrystallized quartz grain size piezometry (Stipp & Tullis, 2003), the quartz flow law of Hirth et al. (2001), and deformation at 500°C, this range of grain sizes yields shear stresses of 30–59 MPa (average 40 MPa) and strain rates of 7.9×10^{-11}–1.1×10^{-9} s^{-1} (average 2.3×10^{-10} s^{-1}). These estimated shear stresses and strain rates are higher than 10–30 MPa stress and $\sim 10^{-12}$ s^{-1} strain rate estimates for the surrounding metabasite (Tulley et al., 2020). The relatively high shear stresses and presence of coarse metasomatically grown albite of $\sim$1–2 mm in size imply that grain boundary diffusion creep of metasomatic albite is unlikely to occur in the Nishikashiyama mélange (Figure 11). Instead, metasomatized, albite-rich metapelite is incorporated into a viscous CAS matrix as relatively rigid blocks that become dismembered (Figure 8b).

5.3. Relating Metasomatism-Related Deformation to Megathrust Slip

In the Makimine mélange, shear is concentrated along metasomatic, albite-actinolite-rich zones along metapelite-metabasalt/metadolerite boundaries. This is unlikely to occur purely by frictional sliding, because the frictional strengths of actinolite and amphibolite schist are comparable to Byerlee frictional strength (Smith & Faulkner, 2010; Tesei et al., 2012). Shear deformation experiments on powdered basalt with added water demonstrated a decrease in shear strength related to amphibole-forming hydration reactions with a strain rate-stress relationship consistent with diffusion creep (Getsinger & Hirth, 2014). The actinolite and albite fabrics formed by shear within and around the metasomatized metapelite-metabasalt/metadolerite contact zones (Figures 6d and 6g) are strikingly similar to the experimentally generated fabrics (Getsinger & Hirth, 2014). In addition, the very fine grain size (8.6 ± 3.0 μm) of metasomatic albite is favorable for grain boundary diffusion creep (Figure 11). These features are consistent with reaction-enhanced weakening and diffusion creep at reduced stresses in viscous shear zones associated with metasomatic reactions in the Makimine mélange.

Penetrative foliations in metapelite and metabasalt in the Makimine mélange developed under conditions where rheology was controlled by dissolution-precipitation creep and minor crystal plasticity (Needham & Mackenzie, 1988; Tulley et al., 2020, 2022; Ujiie et al., 2018). Metasomatic albite locally overprinted the mélange foliation along the interfaces between metapelite and metabasalt/metadolerite (Figures 2b and 2d). These features suggest that megathrust shear was accommodated by distributed shear across the penetrative mélange foliations as well as within localized metasomatism-related viscous shear zones. The temperature range of the observed albitization in the Makimine mélange and the hydrothermal experiments of Rosenbauer et al. (1983) suggest that albite metasomatism of the metapelite potentially begins to occur at $\sim$350°C, corresponding to the temperature at the downdip limit of the seismogenic zone (Hyndman et al., 1997). Thus, when multiple metasomatism-related viscous shear zones accommodated megathrust shear, weakening and diffusion creep associated with metasomatic reactions and grain size reduction could contribute to decreased megathrust strength near the seismic-aseismic transition. The calculated shear stress in the reaction zones is comparable to strengths of adjacent hydrous metabasalt and mica schist at peak *P-T* conditions of the Makimine mélange (Shea & Kronenberg, 2009; Tulley et al., 2020), and somewhat higher than strengths during pressure solution creep of metasediments deformed at similar *T* in the Arosa Zone in the Alps (Condit et al., 2022).

In the Nishikashiyama mélange, mutually crosscutting relationship between viscous shear structures and quartz veins in CAS indicates episodic fracturing during dominantly viscous shear. CPO patterns demonstrate activation of quartz prism [c] slip (Figure 9d) that, although typically a higher temperature mechanism, has been documented at somewhat warmer conditions than the Nishikashiyama mélange ($\sim$550–600°C) under hydrous conditions (Mainprice et al., 1986; Okudaira et al., 1995). H_2O and silica release during albitization (Figure 5d) could contribute to the local formation of quartz veins and to fill the fractures formed by pore space generation related to the estimated $\sim$14% volume loss during albitization. Local occurrence of subgrain rotation recrystallization in quartz within CAS is in contrast with predominance of grain boundary migration recrystallization in surrounding rocks. These differences in microstructure and approximately two orders of magnitude higher strain rate in CAS relative to the surrounding metabasite (Tulley et al., 2020) are consistent with increased strain rate along CAS (Stipp et al., 2002). This strain localization into CAS could either result from stress concentration near

the stronger metabasite and metasomatized metapelite or from a relative weakness of the CAS or combination of these factors.

As in the case of the Makimine mélange, the Nishikashiyama mélange also recorded changes in the deformation style during subduction. Distributed shear along metamorphic foliations was mainly accommodated by dissolution-precipitation creep coupled to slip along phyllosilicates (Tulley et al., 2020), and foliations are locally folded. In contrast, metasomatism-related viscous shear was localized along multiple CAS horizons that are traceable over the size of the outcrops and metasomatic albite overprinted the foliations (Figures 4c and 4d). As such, although volumetrically minor, CAS represents a potential interconnected zone of localized sliding that may accommodate megathrust slip. If megathrust slip was accommodated by the 50-m-thick Nishikashiyama mélange (Nishiyama, 1989) and deformed at a strain rate of 2.3×10^{-10} s^{-1}, the slip rate was ~1 mm/day, comparable to slow slip rates below the seismogenic zone (Behr & Bürgmann, 2021 and references therein). Approximately three orders of magnitude faster strain rates along localized viscous shear zones within the Nishikashiyama mélange, compared to those in the Makimine mélange, may represent relatively fast, transient SSEs, and relatively slow, steady creep, respectively. Comparable increases in strain rate have been calculated for strain localization in lower crustal mylonitized pseudotachylytes and interpreted as resulting from afterslip (Campbell & Menegon, 2019). However, lack of evidence for seismic precursors makes SSEs a more likely source of locally elevated strain rates in the Nishikashiyama mélange, although pseudotachylytes readily suffer from subsequent alteration and crystal-plastic deformation (Kirkpatrick & Rowe, 2013; Ujiie & Kimura, 2014).

Quartz vein formation in locations of metamorphic dehydration within the dominantly viscous regime could explain the tremor signal commonly observed alongside SSEs (Fagereng et al., 2018; Fisher & Brantley, 2014; Tulley et al., 2022; Ujiie et al., 2018). Quartz veins, related to H_2O and silica release from the metapelite during metasomatic reactions that potentially generate pore space through volume loss (Figure 5d), may also be involved in tremor-forming processes as may metasomatic reactions involving interaction between the mantle wedge and subducting sediments (Tarling et al., 2019). Silica release during metasomatism may also contribute increased silica content in metabasite immediately below CAS (Table 2); such features are absent in metadolerite nearby the metasomatic reaction zone in the Makimine mélange, where silica contents remained unchanged during metasomatism (Table 1 and Figure 3d).

In contrast to very fine grained albite at conditions of the base of the seismogenic zone at ~350°C, the albite metasomatism at greater depths and temperature of ~500°C produced coarse-grained albite. The rheological effect of metasomatic albitization reactions therefore varies with depth and temperature along the megathrust; fault weakening by grain-boundary diffusion creep in very fine-grained reaction products at the base of the seismogenic zone was replaced at greater depth by the formation of a relatively strong material mainly composed of coarse-grained albite, forming relatively rigid blocks in a weaker foliated matrix. The rheological differences may also arise between metabasite/metapelite blocks and the weaker CAS matrix. Brittle-viscous deformation in such heterogeneous geological assemblages has been suggested as a mechanism to produce ETS (Ando et al., 2012; Beall et al., 2019; Behr et al., 2018; Fagereng et al., 2014; Hayman & Lavier, 2014; Skarbek et al., 2012).

6. Conclusions

We studied subduction mélanges exhumed from downdip of the seismogenic zone to clarify how metasomatic reactions affect changes in the megathrust slip mode with depth. The mélanges recorded albite metasomatism between juxtaposed metapelite and metabasaltic rocks, which could modulate the rheology of megathrust slip. Mineralogical and chemical changes during metasomatic reactions as well as field observations suggest that albite metasomatism occurred at temperatures exceeding ~350°C. In a mélange deformed at ~370°C, grain boundary diffusion creep facilitated by very fine grained metasomatic albite can potentially contribute to low flow stresses around the thermally inferred base of the seismogenic zone, but creates a minor viscosity contrast. Deeper, in a mélange deformed at ~500°C near the mantle wedge corner, albite metasomatism facilitated local quartz vein formation and localized viscous shear at an increased strain rate under hydrous conditions, during which coarse-grained metasomatic products increase local viscosity contrast and behave as relatively rigid blocks in a viscous matrix. This could be a mechanism for strain localization resulting in deep SSEs with tremor.

Data Availability Statement

The Electron backscatter diffraction data used to determine quartz and albite grain size are available at https://doi.org/10.5281/zenodo.6609387.

References

Ague, J. J. (2011). Extreme channelization of fluid and the problem of element mobility during Barrovian metamorphism. *American Mineralogist*, *96*(2–3), 333–352. https://doi.org/10.2138/am.2011.3582

Ando, R., Takeda, N., & Yamashita, T. (2012). Propagation dynamics of seismic and aseismic slip governed by fault heterogeneity and Newtonian rheology. *Journal of Geophysical Research*, *117*(B11), B11308. https://doi.org/10.1029/2012JB009532

Angiboust, S., Kirsch, J., Oncken, O., Goldny, J., Monié, P., & Rybacki, E. (2015). Probing the transition between seismically coupled and decoupled segments along an ancient subduction interface. *Geochemistry, Geophysics, Geosystems*, *16*(6), 1905–1922. https://doi.org/10.1002/2015GC005776

Audet, P., & Bürgmann, R. (2014). Possible control of subduction zone slow-earthquake periodicity by silica enrichment. *Nature*, *510*(7505), 389–392. https://doi.org/10.1038/nature13391

Baumgartner, L. P., & Olsen, S. N. (1995). A least-squares approach to mass transport calculations using the isocon method. *Economic Geology*, *90*, 1261–1270. https://doi.org/10.2113/gsecongeo.90.5.1261

Beall, A., Fagereng, Å., & Ellis, S. (2019). Fracture and weakening of jammed subduction shear zones, leading to the generation of slow slip events. *Geochemistry, Geophysics, Geosystems*, *20*(11), 4869–4884. https://doi.org/10.1029/2019GC008481

Bebout, G. E. (2007). Metamorphic chemical geodynamics of subduction zones. *Earth and Planetary Science Letters*, *260*(3–4), 373–393. https://doi.org/10.1016/j.epsl.2007.05.050

Bebout, G. E., & Penniston-Dorland, S. C. (2016). Fluid and mass transfer at subduction interfaces-The field metamorphic record. *Lithos*, *240–243*, 228–258. https://doi.org/10.1016/lithos.2015.10.007

Behr, W. M., & Bürgmann, R. (2021). What's down there? The structures, materials and environment of deep-seated slow slip and tremor. *Philosophical Transactions of the Royal Society A*, *379*(2193), 20200218. https://doi.org/10.1098/rsta.2020.0218

Behr, W. M., Kotowski, A. J., & Ashley, K. T. (2018). Dehydration-induced rheological heterogeneity and the deep tremor source in warm subduction zones. *Geology*, *45*(5), 475–478. https://doi.org/10.1130/G40105.1

Beroza, G. C., & Ide, S. (2011). Slow earthquakes and nonvolcanic tremor. *Annual Review of Earth and Planetary Sciences*, *39*(1), 271–296. https://doi.org/10.1146/annurev-earth-040809-152531

Beyssac, O., Goffé, B., Chopin, C., & Rouzaud, J. N. (2002). Raman spectra of carbonaceous material in metasediments: A new geothermometer. *Journal of Metamorphic Geology*, *20*(9), 859–871. https://doi.org/10.1046/j.1525-1314.2002.00408.x

Campbell, L. R., & Menegon, L. (2019). Transient high strain rate during localized viscous creep in the dry lower continental crust (Lofoten, Norway). *Journal of Geophysical Research: Solid Earth*, *124*(10), 10240–10260. https://doi.org/10.1029/2019JB018052

Condit, C. B., French, M. E., Hayles, J. A., Yeung, L. Y., Chin, E. J., & Lee, C.-T. A. (2022). Rheology of metasedimentary rocks at the base of the subduction seismogenic zone. *Geochemistry, Geophysics, Geosystems*, *23*(2), e2021GC010194. https://doi.org/10.1029/2021GC010194

Fagereng, Å., & Den Hartog, S. A. (2017). Subduction megathrust creep governed by pressure solution and frictional-viscous flow. *Nature Geoscience*, *10*(1), 51–57. https://doi.org/10.1038/ngeo02857

Fagereng, Å., Diener, J. F. A., Meneghini, F., Harris, C., & Kvadsheim, A. (2018). Quartz vein formation by local dehydration embrittlement along the deep, tremorgenic subduction thrust interface. *Geology*, *46*(1), 67–70. https://doi.org/10.1130/G39649.1

Fagereng, Å., Hillary, G. W. B., & Diener, J. F. A. (2014). Brittle-viscous deformation, slow slip, and tremor. *Geophysical Research Letters*, *41*(12), 4159–4167. https://doi.org/10.1002/2014GL060433

Faure, M., Fabbri, O., & Monie, P. (1988). The miocene bending of southwest Japan: New ^{39}Ar/^{40}Ar and microtectonic constraints from the nagasaki schists (Western Kyushu), an extension of the sanbagawa high-pressure belt. *Earth and Planetary Science Letters*, *91*(1–2), 105–116. https://doi.org/10.1016/0012-821X(88)90154-9

Fisher, D. M., & Brantley, S. L. (2014). The role of silica redistribution in the evolution of slip instabilities along subduction interfaces: Constraints from the Kodiak accretionary complex, Alaska. *Journal of Structural Geology*, *69*, 395–414. https://doi.org/10.1016/j.jsg.2014.03.010

Fitz Gerald, J. D., Etheridge, M. A., & Vernon, R. H. (1983). Dynamic recrystallization in a naturally deformed albite. *Texture, Stress, and Microstructure*, *5*(4), 219–237. https://doi.org/10.1155/TSM.5.219

Gao, X., & Wang, K. (2017). Rheological separation of the megathrust seismogenic zone and episodic tremor and slip. *Nature*, *543*(7645), 416–419. https://doi.org/10.1038/nature21389

Getsinger, A. J., & Hirth, G. (2014). Amphibole fabric formation during diffusion creep and the rheology shear zones. *Geology*, *42*(6), 535–538. https://doi.org/10.1130/G35327.1

Grant, J. A. (1986). The isocon diagram-a simple solution to Gresens' equation for metamorphic alteration. *Economic Geology*, *81*(8), 1976–1982. https://doi.org/10.2113/gseconger.81.8.1976

Grant, J. A. (2005). Isocon analysis: A brief review of the method and applications. *Physics and Chemistry of the Earth*, *30*(17–18), 997–1004. https://doi.org/10.1016/j.pce.2004.11.003

Hara, H., & Kimura, K. (2008). Metamorphic and cooling history of the Shimanto accretionary complex, Kyushu, southwest Japan: Implications for the timing of out-of-sequence thrusting. *Island Arc*, *17*(4), 546–559. https://doi.org/10.1111/j.1440-1738.2008.00636.x

Hattori, H., & Shibata, K. (1982). Radiometric dating of pre-Neogene granitic and metamorphic rocks in northwest Kyushu, Japan-with emphasis on geotectonics of the Nishisonogi zone. *Bulletin of the Geological Survey of Japan*, *33*, 57–84.

Hayman, N. W., & Lavier, L. L. (2014). The geologic record of deep episodic tremor and slip. *Geology*, *42*(3), 195–198. https://doi.org/10.1130/G34990.1

Heinemann, S., Wirth, R., Gottschalk, M., & Dresen, G. (2005). Synthetic [100] tilt grain boundaries in forsterite: 9.9 to 21.5. *Physics and Chemistry of Minerals*, *32*(4), 229–240. https://doi.org/10.1007/s00269-005-0448-9

Hirth, G., Teyssier, C., & Dunlap, W. J. (2001). An evaluation of quartzite flow laws based on comparisons between experimentally and naturally deformed rocks. *International Journal of Earth Sciences*, *90*(1), 77–87. https://doi.org/10.1007/s005310000152

Hyndman, R. D., Yamano, M., & Oleskevich, D. A. (1997). The seismogenic zone of subduction thrust faults. *Island Arc*, *6*(3), 244–260. https://doi.org/10.1111/j.1440-1738.1997.tb00175.x

Johnson, J. W., Oelkers, E. H., & Helgeson, H. C. (1992). SUPCRT92: A software package for calculating the standard molal thermodynamic properties of minerals, gases, aqueous species, and reactions from 1 to 5000 bar and 0 to 1000°C. *Computers & Geosciences*, *18*(7), 899–947. https://doi.org/10.1016/0098-3004(92)90029-Q

Kagi, H., Tsuchida, I., Wakatsuki, M., Takahashi, K., Kamimura, N., Iuchi, K., & Wada, H. (1994). Proper understanding of down-shifted Raman spectra of natural graphite: Direct estimation of laser-induced rise in sample temperature. *Geochimica et Cosmochimica Acta*, *58*(16), 3527–3530. https://doi.org/10.1016/0016-7037(94)90104-X

Kawano, S., Katayama, I., & Okazaki, K. (2011). Permeability anisotropy of serpentinite and fluid pathways in a subduction zone. *Geology*, *39*(10), 939–942. https://doi.org/10.1130/G32173.1

Kirkpatrick, J. D., & Rowe, C. D. (2013). Disappearing ink: How pseudotachylytes are lost from the rock record. *Journal of Structural Geology*, *52*, 183–198. https://doi.org/10.1016/j.jsg.2013.03.003

Kouketsu, Y., Mizukami, T., Mori, H., Endo, S., Aoya, M., Hara, H., et al. (2014). A new approach to develop the Raman carbonaceous material geothermometer for low-grade metamorphism using peak width. *Island Arc*, *23*(1), 33–50. https://doi.org/10.1111/iar.12057

Lahfid, A., Beyssac, O., Deville, E., Negro, F., Chopin, C., & Goffé, B. (2010). Evolution of the Raman spectrum of carbonaceous material in low-grade metasediments of the Glarus Alps (Switzerland). *Terra Nova*, *22*(5), 354–360. https://doi.org/10.1111/j.1365-3121.2010.00956.x

Mackenzie, J. S., Needham, D. T., & Agar, S. M. (1987). Progressive deformation in an accretionary complex: An example from the Shimanto belt of eastern Kyushu, southwest Japan. *Geology*, *15*(4), 353–356. https://doi.org/10.1130/0091-7613(1987)15<353:PDIAAC>2.0.CO;2

Mainprice, D., Bouchez, J.-L., Blumenfeld, P., & Tubá, J. M. (1986). Dominant *c* slip in naturally deformed quartz: Implications for dramatic plastic softening at high temperature. *Geology*, *14*(10), 819–822. https://doi.org/10.1130/0091-7613(1986)14<819:DCSIND>>2.0.CO;2

Matsumura, M., Hashimoto, Y., Kimura, G., Ohmori-Ikehara, K., Enjohji, M., & Ikesawa, E. (2003). Depth of oceanic-crust underplating in a subduction zone: Inferences from fluid-inclusion analyses of crack-seal veins. *Geology*, *31*(11), 1005–1008. https://doi.org/10.1130/G19885.1

Mori, Y., & Mashima, H. (2005). X-ray fluorescene analysis of major and trace elements in silicate rocks using 1:5 dilution glass beads. *Bulletin of the Kitakyushu Museum of Natural History and Human History Series A Natural History*, *3*, 1–12.

Mori, Y., Shigeno, M., Miyazaki, K., & Nishiyama, T. (2019). Peak metamorphic temperature of the Nishisonogi unit of the Nagasaki metamorphic rocks, Western Kyushu, Japan. *Journal of Mineralogical and Petrological Sciences*, *114*(4), 170–177. https://doi.org/10.2465/jmps.190423

Mori, Y., Shigeno, M., & Nishiyama, T. (2014). Fluid-metapelite interaction in an ultramafic mélange: Implications for mass transfer along the slab-mantle interface in subduction zones. *Earth Planets and Space*, *66*(1), 47. https://doi.org/10.1186/1880-5981-66-47

Müller, R. D., Sdrolias, M., Gaiana, C., Steinberger, B., & Heine, C. (2008). Long-term sea-level fluctuations driven by ocean basin dynamics. *Science*, *319*(5868), 1357–1362. https://doi.org/10.1126/science.1151540

Needham, D. T., & Mackenzie, J. S. (1988). Structural evolution of the Shimanto belt accretionary complex in the area of the Gokase River, Kyushu, SW Japan. *Journal of the Geological Society*, *145*(1), 85–94. https://doi.org/10.1144/gsjgs.145.1.0085

Nishiyama, N., Sumino, H., & Ujiie, K. (2020). Fluid overpressure in subduction plate boundary caused by mantle-derived fluids. *Earth and Planetary Science Letters*, *538*, 116199. https://doi.org/10.1016/j.epsl.2020.116199

Nishiyama, T. (1989). Petrologic study of the Nagasaki metamorphic rocks in the Nishisonogi Peninsula-with special reference to the greenrock complex and the reaction-enhanced ductility. *Memoirs of the Geological Society of Japan*, *33*, 237–257.

Nishiyama, T. (1990). CO_2-metasomatism of a metabasite block in a serpentine mélange from the Nishisonogi metamorphic rocks, southwest Japan. *Contributions to Mineralogy and Petrology*, *104*(1), 35–46. https://doi.org/10.1007/BF00310644

Noda, H., & Lapusta, N. (2013). Stable creeping fault segments can become destructive as a result of dynamic weakening. *Nature*, *493*(7433), 518–521. https://doi.org/10.1038/nature11703

Obara, K., Hirose, H., Yamamizu, F., & Kasahara, K. (2004). Episodic slow slip events accompanied by non-volcanic tremors in southwest Japan subduction zone. *Geophysical Research Letters*, *31*(23), L23602. https://doi.org/10.1029/2004GL020848

Obara, K., & Kato, A. (2016). Connecting slow earthquakes to huge earthquakes. *Science*, *353*(6296), 253–257. https://doi.org/10.1126/science.aaf1512

Offerhaus, L. J., Wirth, R., & Dresen, G. (2001). High-temperature creep of polycrystalline albite. *Deformation mechanisms, rheology and tectonics*, *124*, 107–131.

Okamoto, A., Oyanagi, R., Yoshida, K., Uno, M., Shimizu, H., & Satish-Kumar, M. (2021). Rupture of wet mantle wedge by self-promoting carbonation. *Communications Earth & Environment*, *2*(1), 151. https://doi.org/10.1038/s43247-021-00224-5

Okudaira, T., Takeshita, T., Hara, I., & Ando, J. (1995). A new estimate of the conditions for transition from basal <a> to prism [c] slip in naturally deformed quartz. *Tectonophysics*, *250*(1–3), 31–46. https://doi.org/10.1016/0040-1951(95)00039-4

Palazzin, G., Raimbourg, H., Famin, V., Jolivet, L., Kusaba, Y., & Yamaguchi, A. (2016). Deformation processes at the down-dip limit of the seismogenic zone: The example of Shimanto accretionary complex. *Tectonophysics*, *687*, 28–43. https://doi.org/10.1016/j.tecto.2016.08.013

Peng, Z., & Gomberg, J. (2010). An integrated perspective of the continuum between earthquakes and slow slip phenomena. *Nature Geoscience*, *3*(9), 599–607. https://doi.org/10.1038/ngeo940

Prior, D. J., Boyle, A. P., Brenker, F., Cheadle, M. C., Day, A., Lopez, G., et al. (1999). The application of electron backscatter diffraction and orientation contrast imaging in the SEM to textural problems in rocks. *American Mineralogist*, *84*(11–12), 1741–1759. https://doi.org/10.2138/am-1999-11-1204

Raimbourg, Z. H., Famin, V., Palazzin, G., Mayoux, M., Jolivet, L., Ramboz, C., & Yamaguchi, A. (2018). Fluid properties and dynamics along the seismogenic plate interface. *Geosphere*, *14*(2), 469–491. https://doi.org/10.1130/GES01504.1

Rogers, G., & Dragert, H. (2003). Episodic tremor and slip on the Cascadia subduction zone: The chatter of silent slip. *Science*, *300*(5627), 1942–1943. https://doi.org/10.1126/science.1084783

Rollinson, H. (1993). *Using geochemical data: Evaluation, presentation, interpretation* (p. 352). Longman.

Rosenbauer, R. J., Bischoff, J. L., & Radtke, A. S. (1983). Hydrothermal alteration of graywacke and metabasite by 4 molal NaCl. *Economic Geology*, *78*(8), 1701–1710. https://doi.org/10.2113/gsecongeo.78.8.1701

Shea, W. T., & Kronenberg, A. K. (2009). Rheology and deformation mechanisms of an isotropic mica schist. *Journal of Geophysical Research*, *97*(B11), 15201–15237. https://doi.org/10.1029/92JB00620

Shigematsu, N., Prior, D. J., & Wheeler, J. (2006). First combined electron backscatter diffraction and transmission electron microscopy study of grain boundary structure of deformed quartzite. *Journal of Microscopy*, *224*(3), 306–321. https://doi.org/10.1111/j.1365-2818.2006.01697.x

Skarbek, R. M., Rempel, A. W., & Schmidt, D. A. (2012). Geologic heterogeneity can produce aseismic slip transients. *Geophysical Research Letters*, *39*(21), L21306. https://doi.org/10.1029/2012GL053762

Smith, S. A. F., & Faulkner, D. R. (2010). Laboratory measurements of the frictional properties of the Zuccale low-angle normal fault, Elba Island, Italy. *Journal of Geophysical Research*, *115*(B2), B02407. https://doi.org/10.1029/2008JB006274

Stipp, M., Stünitz, H., Heilbronner, R., & Schmid, S. M. (2002). Dynamic recrystallization of quartz: Correlation between natural and experimental conditions. In de Meer, S., et al. (Eds.). *Deformation mechanisms, rheology and tectonics: Current status and future perspectives* (Vol. 200, pp. 171–190). Geological Society, London, Special Publications. https://doi.org/10.1144/GSL.SP.2001.200.01.11

Stipp, M., & Tullis, J. (2003). The recrystallized grain size piezometer for quartz. *Geophysical Research Letters*, *30*(21), 2088. https://doi.org/10.1029/2003GL018444

Sun, S. S., & McDonough, W. F. (1989). Chemical and isotopic systematics of oceanic basalts; implications for mantle compositions and processes. *Geological Society, London, Special Publications*, *42*(1), 313–345. https://doi.org/10.1144/GSL.SP.1989.042.01.19

Tarling, M. S., Smith, S. A. F., & Scott, J. M. (2019). Fluid overpressure from chemical reactions in serpentinite within the source region of deep episodic tremor. *Nature Geoscience*, *12*, 1034–1042. https://doi.org/10.1038/s41561-019-0470-z

Tesei, T., Collettini, C., Carpenter, B. M., Viti, C., & Marone, C. (2012). Frictional strength and healing behavior of phyllosilicate-rich faults. *Journal of Geophysical Research*, *117*(B9), B09402. https://doi.org/10.1029/2012JB009204

Toriumi, M., & Teruya, J. (1988). Tectono-metamorphism of the Shimanto belt. *Modern Geology*, *12*, 303–324.

Tulley, C. J., Fagereng, Å., & Ujiie, K. (2020). Hydrous oceanic crust hosts megathrust creep at low shear stresses. *Science Advances*, *6*(22), eaba1529. https://doi.org/10.1126/sciadv.aba1529

Tulley, C. J., Fagereng, Å., Ujiie, K., Diener, J. F. A., & Harris, C. (2022). Embrittlement within viscous shear zones across the base of the subduction thrust seismogenic zone. *Geochemistry, Geophysics, Geosystems*, *23*, e2021GC010208. https://doi.org/10.1029/2021gc010208

Ujiie, K., & Kimura, G. (2014). Earthquake faulting in subduction zones: Insights from fault rocks in accretionary prisms. *Progress in Earth and Planetary Science*, *1*(1), 7. https://doi.org/10.1186/2197-4284-1-7

Ujiie, K., Saishu, H., Fagereng, Å., Nishiyama, N., Otsubo, M., Masuyama, H., & Kagi, H. (2018). An explanation of episodic tremor and slow slip constrained by crack-seal veins and viscous shear in subduction mélange. *Geophysical Research Letters*, *45*(11), 5371–5379. https://doi.org/10.1029/2018GL078374

White, S. (1976). The effects of strain on the microstructures, fabric, and deformation mechanisms in quartzites. *Philosophical Transactions of the Royal Society of London,Series A*, *283*, 69–86. https://doi.org/10.1098/rsta.1976.0070

Whittaker, L. M., Müller, R. D., Leitchenkov, H., Stagg, H., Sdrolias, M., Gaina, C., & Goncharov, A. (2007). Major Australian-Antarctic plate reorganization at Hawaiian-Emperor bend time. *Science*, *318*(5847), 83–86. https://doi.org/10.1126/science.1143769

Yardley, B. W., & Graham, J. T. (2002). The origins of salinity in metamorphic fluids. *Geofluids*, *2*(4), 249–256. https://doi.org/10.1046/j.1468-8123.2002.00042.x

You, C.-F., & Gieskes, J. M. (2001). Hydrothermal alteration of hemi-pelagic sediments: Experimental evaluation of geochemical processes in shallow subduction zones. *Applied Geochemistry*, *16*(9–10), 1055–1066. https://doi.org/10.1016/S0883-2927(01)00024-5